AD_____

Award Number: DAMD17-00-1-0429

TITLE: Radiolabeled Herceptin to Increase Treatment Efficacy
in Breast Cancer Patients with Low tumor HER-2/neu
Expression

PRINCIPAL INVESTIGATOR: Doctor David Scheinberg

CONTRACTING ORGANIZATION: Sloan-Kettering Institute
for Cancer Research
New York, New York 10021

REPORT DATE: July 2004

TYPE OF REPORT: Annual

PREPARED FOR: U.S. Army Medical Research and Materiel Command
Fort Detrick, Maryland 21702-5012

DISTRIBUTION STATEMENT: Approved for Public Release;
Distribution Unlimited

The views, opinions and/or findings contained in this report are
those of the author(s) and should not be construed as an official
Department of the Army position, policy or decision unless so
designated by other documentation.

20050315 038

REPORT DOCUMENTATION PAGE

1. AGENCY USE ONLY (Leave blank)	2. REPORT DATE July 2004	3. REPORT TYPE AND DATES COVERED Annual (15 Jun 03 – 14 Jun 04)

4. TITLE AND SUBTITLE
Radiolabeled Herceptin to Increase Treatment Efficacy in Breast Cancer Patients with Low tumor HER-2/neu Expression

5. FUNDING NUMBERS
DAMD17-00-1-0429

6. AUTHOR(S)
Doctor David Scheinberg

7. PERFORMING ORGANIZATION NAME(S) AND ADDRESS(ES)
Sloan-Kettering Institute for Cancer Research
New York, New York 10021

E-Mail: scheinbd@mskcc.org

8. PERFORMING ORGANIZATION REPORT NUMBER

9. SPONSORING / MONITORING AGENCY NAME(S) AND ADDRESS(ES)
U.S. Army Medical Research and Materiel Command
Fort Detrick, Maryland 21702-5012

10. SPONSORING / MONITORING AGENCY REPORT NUMBER

11. SUPPLEMENTARY NOTES

12a. DISTRIBUTION / AVAILABILITY STATEMENT
Approved for Public Release; Distribution Unlimited

12b. DISTRIBUTION CODE

13. ABSTRACT (Maximum 200 Words)

The primary objective of the proposal is to evaluate the efficacy and feasibility of using radiolabeled Herceptin antibody to target rapidly accessible breast carcinoma cells or micrometastases. By using Herceptin to specifically deliver radiation we anticipate that the efficacy of Herceptin will be extended to include breast cancer cells that are not high HER-2/neu antigen expressors. This hypothesis will be tested using the spheroid model to simulate rapidly accessible micrometastases. An alpha-particle emitting radionuclide will be used to enhance tumor cell kill. Completion of tasks 1-3 and progress towards task 5 was reported in the previous annual report. The animal model previously used towards task 5 was a HER-2/neu expressing ovarian carcinoma. The PI has identified an appropriate disseminated breast carcinoma animal model and is using this to satisfy the remaining tasks of the proposal. Because the PI relocated in 2003, progress in the past year has been delayed. A sub-contract was established with Hopkins to complete the tasks of the proposal. The sub-contract mechanism is being used because after discussions with the contracting officer this was deemed the most expeditious approach to providing funds for the PI to complete the work at Hopkins

14. SUBJECT TERMS
Herceptin, HER-2/neu, alpha particle emitters, Bi-213, Micrometastases

15. NUMBER OF PAGES
35

16. PRICE CODE

17. SECURITY CLASSIFICATION OF REPORT Unclassified	18. SECURITY CLASSIFICATION OF THIS PAGE Unclassified	19. SECURITY CLASSIFICATION OF ABSTRACT Unclassified	20. LIMITATION OF ABSTRACT Unlimited

Table of Contents

INTRODUCTION

In combination with chemotherapy, the antitumor activity of Herceptin (anti-Her-2/neu), a humanized monoclonal antibody directed against HER-2/neu, has been effective in treatment of breast cancer cells overexpressing HER-2/neu. This promising, FDA approved, and commercially available antibody may be effective in eradicating pre-vascularized micormetastatic disease when labeled with a short lived alpha particle emitter. Alpha particles are very effective in sterilizing cells, and 1 to 3 particles transversing the cell is enough for cell kill. Therefore, this treatment approach may have the potential of eradicating micrometastatic disease both of non-overexpressing and overexpressing breast cancer cells. These hypotheses will be tested first on a tumor spheroid model that can be closely controlled. Spheroids of breast cancer cells expressing different levels of HER-2/neu will be incubated with Herceptin labeled with an alpha particle emitting radionuclide. This model will be used to determine optimal antibody concentration, dose level and treatment schedule. Using the results obtained from the *in vitro* spheroid system, a pilot effort to obtain preliminary data on treatment response *in vivo* will be undertaken. Spheroids will be injected intraperitoneally in athymic mice and response to Bi-213-Herceptin therapy will be monitored using MR imaging. The cells in the injected spheroids will be tagged with a MRI contrast agent. The potential of Dexamethasone to enhance radiosensitivity by increased apoptotic death will be examined. The proposed study may result in a novel treatment approach where Herceptin will be used to eradicate breast cancer micrometastases expressing HER-2/neu.

In the previous reporting period, Tasks 1-3 were reported complete and progress towards task 5 was presented. Progress in this reporting period has been delayed because the PI has moved and is starting a lab at a different institution. Accordingly the PI is currently arranging for a 1 year no-cost extension for the unexpended $22,271 funds remaining. In response to the review of the previous annual report, the PI has identified a disseminated breast tumor model that will be used to satisfy the animal dose-response tasks, instead of the HER-2/neu expressing ovarian carcinoma used previously as a surrogate for disseminated breast cancer. Details regarding the proposed model and methodologies that will be employed are provided below.

BODY

Task 5 (month 25-26) – Select one cell line and inject spheroids in the peritoneal cavity of mice. Determine baseline growth as measured by MRI

As noted in the previous report, the tumor take following injection of the cell lines listed above was inadequate. We, therefore, moved to an ovarian carcinoma model using a cell line with a high HER-2/neu expression. Using this model we completed microPET imaging of ^{86}Y-Herceptin tumor targeting and also MRI tumor characterization. This work was recently published (reportable outcomes - 1). We have identified a more appropriate model and plan on developing this for accomplishing tasks 6 and 7.

Tasks 6 and 7 (months 27-36) – Use optimal Herceptin concentration and Bi-213 activity as determined in the spheroid model and treat spheroids injected intraperitoneally in mice. Follow response by MRI. Treat animals inoculated with spheroids with Herceptin-Bi-213 in combination with DEX to determine if DEX enhances radiosensitivity. Follow response by MRI.

In response to the reviewer's comments on the previous annual report, a metastatic breast cancer model will be used to complete the tasks of the project. Work will be completed at Johns Hopkins University, School of Medicine under a sub-contract from Memorial Sloan-Kettering Cancer Center which will retain the grant under a "caretaker" PI. This approach was chosen after consultation with the contracting officer as being the most expeditious approach to providing the funds for completion of the project. The model that will be used at Hopkins and progress towards characterizing this model is described in the attached summary.

KEY RESEARCH ACCOMPLISHMENTS (prior and current reporting period)

- Generated and characterized the growth of spheroids expressing different levels of HER-2/neu receptor.
- Evaluated the radiosensitivities of the three cell lines used for generating the spheroids.
- Characterized antibody penetration kinetics into HER-2/neu expressing spheroids.
- Evaluated the response of HER-2/neu expressing spheroids to Herceptin and to Ac-225 labeled antibody
- Demonstrated of the feasibility of controlling tumor cell clusters with intermediate expression of HER-2/neu using Ac-225-labeled Herceptin
- Demonstrated microPET imaging of HER-2/neu expressing tumor and MRI-based size determinations
- Identified and characterized a transgenic disseminated breast cancer model for therapeutic studies

REPORTABLE OUTCOMES

Published paper: Palm S, Enmon RM, Matei C, Kolbert KS, Xu S, Pellegrini V, Zanzonico PB, Finn RL, Koutcher JA, Larson SM, Sgouros G. Pharmacokinetics and biodistribution of ^{86}Y-Trastuzumab for ^{90}Y dosimetry in an ovarian carcinoma model: Correlative microPET and MRI. J Nucl Med 2003;44:1148-1155.

Published paper: Ballangrud ÅM, Yang W-H, Palm S, Enmon R, Borchardt PE, Pellegrini VA, McDevitt MR, Scheinberg DA, Sgouros G. Alpha-particle emitting atomic generator (^{225}Ac)-labeled Trastuzumab (Herceptin) targeting of breast cancer spheroids: Efficacy versus HER2/*neu* expression. Clin Cancer Res, In Press.

CONCLUSIONS

Tasks 1-3 have been completed, Preliminary work towards task 5 has been published but will be repeated using a more appropriate, breast-cancer specific model. Remaining tasks will be completed at Johns Hopkins Univeristy, School of Medicine.

Dose-response results obtained with MDA MB361 spheroids suggest that it will be possible to eradicate tumor cells with intermediate expression of HER-2/neu using Ac-225-labeled herceptin at a concentration between 100 and 500 nCi/ml. Scaled up to human administration, assuming an initial distribution volume of 3L (i.e., the plasma volume), this activity concentration translates to approximately a 1 mCi injection of ^{225}Ac-Herceptin. Based on animal studies, this activity concentration is clinically realistic.

SO WHAT? These preliminary studies suggest that by using Herceptin antibody radiolabeled with an alpha-particle emitter it may be possible to treat breast cancer patients whose tumor does not demonstrate high expression of HER-2/neu.

Appendix Material

1. Palm,S., Enmon,R.M., Jr., Matei,C., Kolbert,K.S., Xu,S., Zanzonico,P.B., Finn,R.L., Koutcher,J.A., Larson,S.M., and Sgouros,G. 2003. Pharmacokinetics and Biodistribution of (86)Y-Trastuzumab for (90)Y Dosimetry in an Ovarian Carcinoma Model: Correlative MicroPET and MRI. *J Nucl Med* 44:1148-1155.

2. Ballangrud AM, Yang W-H, Palm S, Enmon R, Borchardt PE, Pellegrini VA, McDevitt MR, Scheinberg DA, Sgouros G. Alpha-particle emitting atomic generator (Ac225)-labeled Herceptin targeting breast cancer spheroids: efficacy versus HER-2/neu expression

Reference List

1. Palm,S., Enmon,R.M., Jr., Matei,C., Kolbert,K.S., Xu,S., Zanzonico,P.B., Finn,R.L., Koutcher,J.A., Larson,S.M., and Sgouros,G. 2003. Pharmacokinetics and Biodistribution of (86)Y-Trastuzumab for (90)Y Dosimetry in an Ovarian Carcinoma Model: Correlative MicroPET and MRI. *J Nucl Med* 44:1148-1155.

Progress Report for DOD grant

The aims of this grant are to develop and evaluate alpha-particle emitter labeled Herceptin antibody to enhance the efficacy of Herceptin antibody therapy in patients with breast cancer and also to increase the population of breast cancer patients that could benefit from targeted therapy. Prior studies used a HER2/neu positive ovarian carcinoma model to demonstrate the potential efficacy of alpha-emitter labeled Herceptin. The PI of this grant recently moved to Johns Hopkins University, School of Medicine and the work is continuing at Johns Hopkins. Administratively, however, the grant has remained at Memorial Sloan-Kettering Cancer Center under an arrangement in which Dr. David Scheinberg, a close collaborator on this work, is the named PI and the work has been sub-contracted to Dr. Sgouros, PI of the application, before the move to Hopkins. As a result of the move, work on this proposal has been delayed by approximately 8 to 9 months, the time required for Dr. Sgouros to establish the lab at Hopkins. This has now been accomplished and studies related to the development of a metastatic breast carcinoma model are presented as well as preliminary cell kill and radiosensitvity studies for ^{213}Bi alphas as well as a mathematical modeling analysis of a potential treatment strategy using alpha-emitter labeled Herceptin; all of the studies presented were performed at Johns Hopkins. The radiosensitivity and modeling studies will be used in the dosimetric analysis of planned efficacy and toxicity studies. The animal model is briefly described below.

We have developed a metastatic breast carcinoma model that expresses HER2/neu and that also exhibits normal organ expression of the antigen. The major advantage of this transgenic model is that unlike a xenograft wherein only the tumor cells express the target antigen, the transgenic model better mimics the conditions of targeted alpha-particle therapy in humans by the presence of cross-reactive normal tissues. This model will be used to perform toxicity and efficacy studies of targeted alpha-emitter therapy. The model is briefly described below.

HER-2/*neu* transgenic (Neu-N) mice (1), express the nontransforming rat *neu* cDNA under the mouse mammary tumor virus promoter (MMTV). As a consequence, these mice exhibit high (+++) expression of neu in the mammary glands and lower (+) expression in other tissues, including the salivary glands, spleen, thymus, and lungs (2). Beginning at approximately 4 to 6 months of age, the mice develop spontaneous mammary adenocarcinomas in a stochastic manner (3-5). The tumors resemble human breast carcinoma in chronology and histology, as well as in their metastatic pattern. In addition, neu-N mice exhibit evidence of immunological tolerance to the neu protein that appears to mimic what is encountered clinically. Since onset of disease occurs after 4 months, a transplantable tumor model was developed using neu-expressing tumor cell lines, designated NT2 and NT5. These cell lines were derived from spontaneous mammary tumors in female neu-N mice. Mammary fat pad or sub-cutaneous injection (5×10^4 cells) of either cell line leads to palpable (>3mm) tumors in 100 % of mice 3 to 4 weeks after tumor inoculation; by 5 to 6 weeks the tumor-associated morbidity requires animal sacrifice(3-5). Using the intraventricular injection approached described by Arguello, et al (6), the PI's lab has extended this model so that 3 to 4 weeks after left cardiac ventricle (LCV) injection of 10^5 NT2 cells, widespread metastases in the liver and bone/bone marrow are observed necessitating animal sacrifice by 4.5 weeks (7). A serially passaged NT2-derived cell line that shows a high propensity for development of lung metastases has also been developed.

Approximately 40 to 50% of LCV injection attempts are successful (bright red bood at syringe tip)and 80% of successful injections lead to bone (Fig. 1a and b) and liver (Fig. 2) metastases.
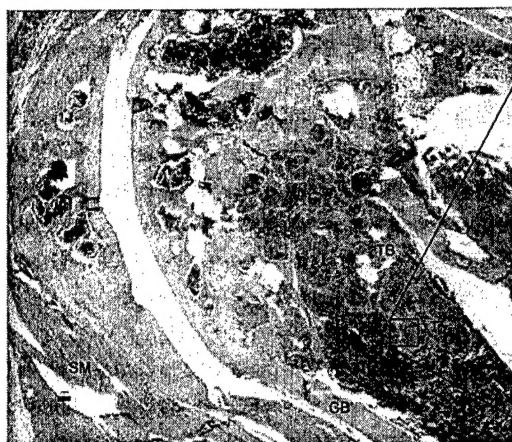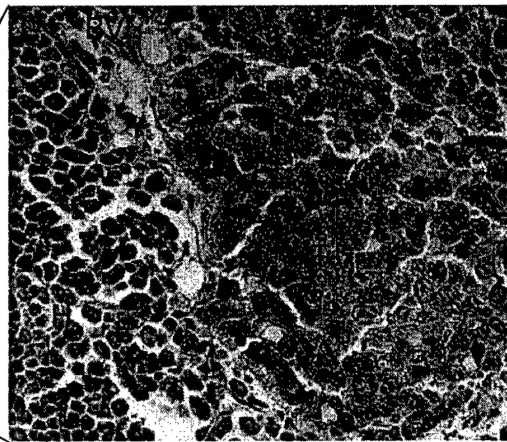
B3 vertebra lysis 50X

B4 vertebra lysis and impinge spinal cord 25X

Fig. 1a. H &E stained histopath sections through the vertebral columns of two different mice, 4 weeks after LCV injection of tumor cells. <u>Left panel</u>: Tumor lysis of vertebral body and invasion into the skeletal muscle. <u>Right panel</u>: tumor extension into the spinal cord region with

B6 femur 25X

B6 femur BM and tumor 400X

Fig 1b. Histopath section through the distal femur 4 wks after LCV injection. <u>Left Panel</u>: Low mag view showing widespread tumor invasion of the marrow cavity. <u>Right Panel</u>: High mag view showing connective tissue and stromal compression (i.e., tumor "capsule") as the tumor met grows

To monitor the formation of tumor metastases, small animal imaging was performed using several different modalities. MicroCT and F-18 fluoride microPET imaging were performed to evaluate skeletal changes. MicroCT images were obtained on an in-house developed imager with an in-plane resolution of 98 μm per pixel. Eight image segments were collected to cover the entire mouse, each segment is 512 x 512 matrix size x 512 slices. Images of a mouse that was later determined, by histopathology, to not have bone mets are depicted to illustrate

the instrumentation and software available to the investigators (Figs. 3). F-18 fluoride μPET imaging was performed to examine the possible use of this approach for monitoring the early onset of bone lesions. F-18 fluoride imaging is expected to highlight regions of bone matrix remodeling, similar to Tc-99m MDP scans. The fluoride ion exchanges with hydroxyl groups in hydroxyapatite crystals of bone. The activity is deposited preferentially at the bone surface and the relative

Fig 2. <u>Left:</u> Gross image of excised liver, 4-weeks after LCV tumor cell injection showing tumor metastases throughout the liver. <u>Right:</u> Section of the liver containing a metastatic tumor mass. At the periphery of the mass is a thick rim of viable tumor cells that infiltrate and compress adjacent hepatic parenchyma. At the center of the mass is a large area of tumor necrosis with remnants of congested vasculture and lesser amounts of hemorrhage and inflammatory cells.
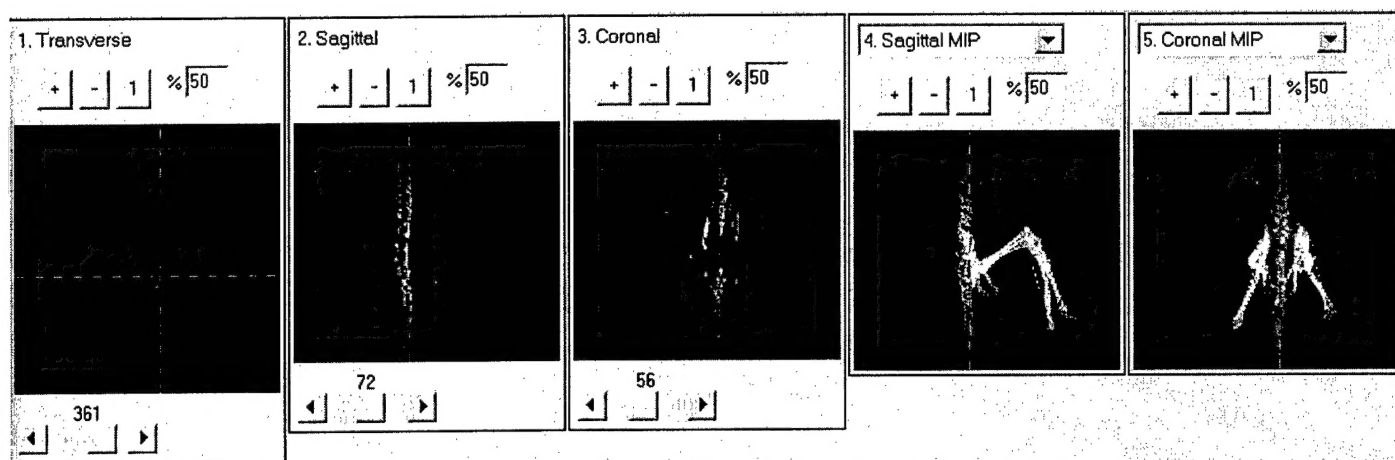
activity of osteoclasts vs osteoblasts is believed to determine [^{18}F]fluoride ion uptake (8). Images are presented to illustrate this modality (Fig. 4). The Atlas μPET was used in these studies.

Fig. 3. microCT sections along the dotted line shown in each view are provided and also sagittal and coronal maximum intensity projection (MIP) views highlighting the bony structure. The image output is obtained from the Multiple Image Analysis Utility (MIAU) software package developed by the PI (Kolbert et al. '98). Using this package, the user may move the cross-hairs to any point in any of the projections and obtain the corresponding images in each view.
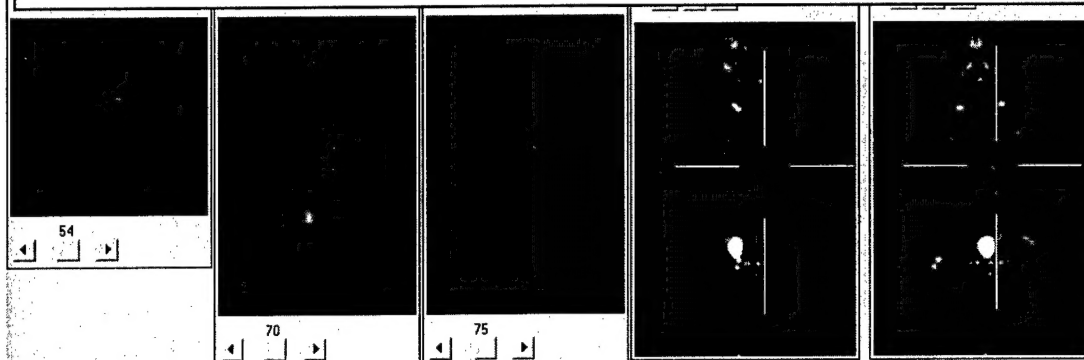

Fig 4. [^{18}F]fluoride microPET images taken 4 weeks after LCV injection of tumor cells showing two focal spots on the spine. (Histopathologic confirmation is pending.) High uptake in the bladder is also observed. The lines indicate the image plane for the sections in panels 1-3.

Micro PET FDG imaging was performed to evaluate the distribution of metastatic disease within mice, as determined by enhanced [^{18}F]fluorodeoxyglucose uptake (Fig. 5).
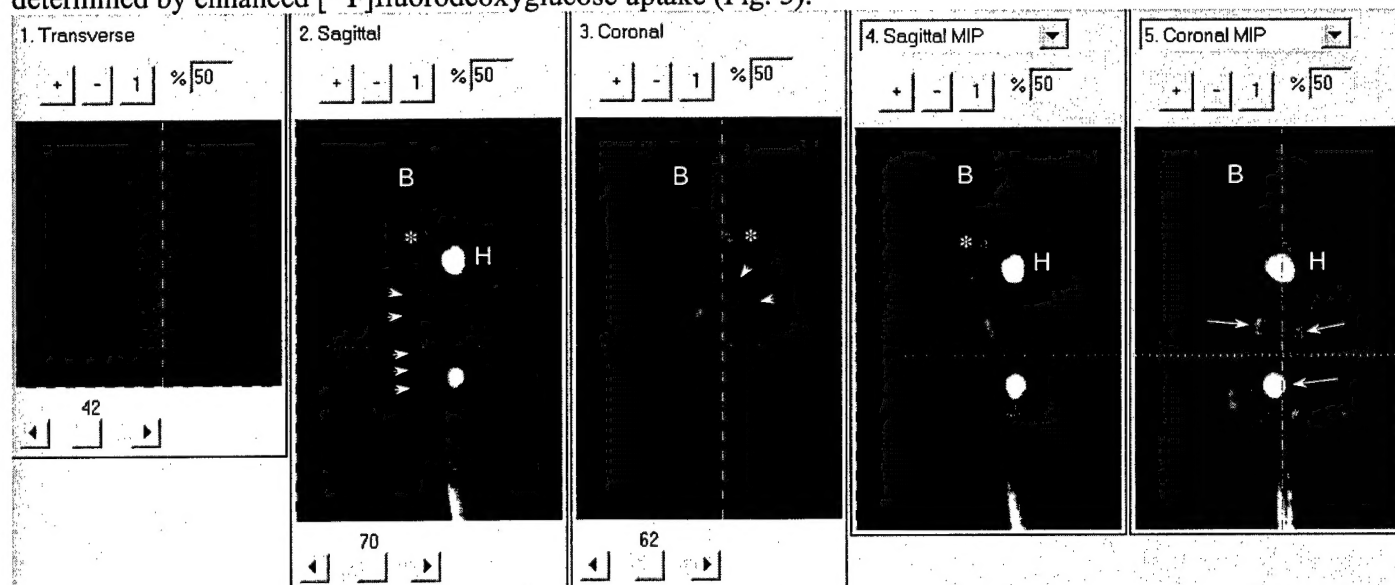

Fig. 5. FDG μPET images of a mouse, 4 weeks after LCV injection of tumor cells. Multiple sites of high uptake are evident along the spinal column (arrowheads, panel 2, sagittal). A coronal slice through the liver, also shows focal uptake in the liver (arrowheads, panel 3, coronal). (The liver of this animal is depicted in Fig. 2.) Consistent with the known high metabolic activity of brain (B) and heart (H), these organs show high uptake. Since FDG is excreted through the urine, the kidneys and bladder are also well visualized (extended arrows in the coronal MIP image, panel 5). Residual activity in the tail is also observed and most, likely represents external contamination of the tail during injection. Likewise, the apparent region of high uptake (*), seen on panels 2 – 4, most likely represents external contamination since no tumor was detected in this region by palpation or by subsequent necropsy of the animal. MRI imaging of this animal confirmed the skeletal metastases, histopath confirmation is pending.

MRI of the mouse shown in Fig. 5 was performed on a 4.7 T unit for anatomical confirmation (Fig. 6) of FDG observations. Images were collected approximately 3 hours after the end of FDG imaging. Over the region imaged, the MR images were consistent with widespread metastases within and emanating from the marrow spaces of the lower vertebral bodies. Tumor was also seen emanating from marrow spaces in the hind limbs. Although not highlighted in figure 5, the multiple regions of focal uptake seen in panel 5 of Fig. 5 are consistent with the images shown on Fig. 6. Upon necropsy, multiple foci of disease were also visible about the hind limbs of this animal. No tumors could be detected by external observation of the mouse. At the time of MR imaging, however, this animal did exhibit hind limb paralysis and also a swollen abdomen, subsequently attributed to ascites accumulation resulting from onset of liver failure (Fig. 2).

slice 2   slice 3   slice 4   slice 5   slice 6   slice 7

Fig. 6. A series of 0.8 mm thick, diffusion-weighted MR image slices showing multiple tumor foci, largely emanating from marrow spaces in both femurs and vertebral bodies. In slices 2 - 4, the region highlighted by the broken contours depicts one such tumor, emanating from the mouse's left hind limb. The well-defined circular region of enhancement contained within the dotted contour shown on slice 3 has a horizontal (shorter) diameter of 3 mm. The rectangular regions in slices 4 and 5 depict tumor emanating from the marrow region of the right hind limb. This is most evident in slice 4 where there is a discontinuity in the zero intensity region (i.e., the bone) surrounding the marrow slit seen near the center of the rectangle. An example of this for disease emanating from marrow within a vertebral body is highlighted by the oval in slice 7. The oval in slice 6 depicts two foci of high intensity that are also most likely originating in the marrow space of vertebral bodies. Despite the large tumor burden, this mouse survived the imaging sessions (T1 weighted images were also collected) and was sacrificed soon after completion of the imaging. Histopathology is pending.

As demonstrated above, the combination of FDG and MR imaging makes it possible to survey the whole body for regions of possible tumor metastases and to then confirm selected sites by MRI. Based on the imaging studies performed to date (and presented in figures 3 through 6), FDG-μPET and MR imaging will be used to evaluate tumor response, *in vivo*, in selected mice undergoing targeted alpha-emitter therapy.

NT2 Cell Radiosensitivity: The modeling/dosimetry analyses required to translate observations in mice into the human requires an assessment of the radiosensivitity of tumor metastases to alpha-particle irradiation. Survival curves for NT2 cells exposed to alpha and external beam photon irradiation were obtained. 1. External Beam: NT2 cells at about 75% confluence were irradiated with external beam (Gammacell 40 Cesium irradiator; dose-rate = 0.8 Gy/min) at various doses. Cells were then trypsinized and transferred to 25 cm^2 T-flask (6 flasks per dose) at 200-5000 cells/flask depending on dosage. The T-flasks were then incubated at 37 °C for 10 days. Cells were then fixed with 95% ethanol and stained with 1% crystal violet in 95% ethanol. Colonies containing at least 50 cells were counted. 2. Alpha-Particle: NT2 cells were plated at 1.5×10^4 cells/well (3 wells per dose) in square bottom 96 well plates (Falcon 35-3072). Radiolabeled mAb (control, ^{213}Bi labeled IgG) was added to reach activity concentration ranging from 0.01 μCi/ml – 20 μCi/ml. The plate was then incubated at 37 °C for 24 hours. The procedure described above for externally irradiated cells was then followed. A non-specific antibody was used in these studies to simplify conversion from μCi/ml to Gy. With non-specific antibody irradiating plated adherent cells, the mean absorbed dose is simply given by: $A_0/\lambda * E_\alpha * \frac{1}{2}$, where A_0 is the initial ^{213}Bi concentration;
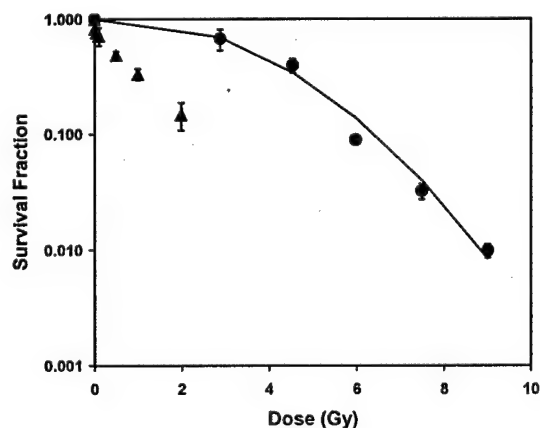

Fig. 8 Cell survival results obtained by colony formation assay are shown; circle = external beam (0.8Gy/min); triangles = ^{213}Bi exposure. The solid line shows a fit of the linear-quadratic model to the data

λ is the physical decay constant (=ln(2)/T$_{1/2}$) for [213]Bi and E$_\alpha$ is the energy emitted as alphas per decay of [213]Bi. The factor of ½ is applied because the cells are adherent and are, therefore, irradiated only from one side. A microdosimetric treatment is not necessary because the concentration of alpha emitters is sufficiently high (9). Cell survival results are summarized in figure 8. The linear quadratic model, SF=exp(-αD-βD^2), was fit to the external beam data, yielding: α=0.0645 Gy^{-1}, β=0.0662 Gy^{-2}, α/β = 0.98 Gy. The α/β value is consistent with late responding tissue, meaning that fractionation of external beam radiation would not be an appropriate strategy for treating tumors derived from this cell line. The alpha-particle curve, on the other hand does not exhibit a shoulder, consistent with the well established failure to repair alpha-particle damage. Fractionation in this situation would be highly effective. A relative biological efficacy (RBE) of 3.5, consistent with published studies of other cell lines (10), is derived from these data.

NT2 spheroid dose-response

The response of NT2 spheroids to [213]Bi alpha-particle irradiation was assessed. Spheroid studies will be used in this work to relate tumor response observed, *in vivo*, to that seen, *in vitro*. The requirement for nutrient and oxygen diffusion limits the maximum distance between viable tumor cells and a vascular supply to approximately 100-200 µm. Correspondingly, initial studies have concentrated on 200 micron diameter spheroids. NT2 tumor cell spheroids were formed and cultivated by liquid overlay culture (11-13). On day 5-7 after inoculation, spheroids with diameters of 200 ± 25 µm were selected and transferred to 35 mm petri dishes. 12 spheroids per plate were used for radiation treatment. Radiolabeled mAb (control, [213]Bi labeled IgG) was added to reach the activity concentrations ranging from 0.2 MBq/ml to 1.0 MBq/ml. The petri dishes were incubated at 37 °C for 24 hours. The spheroids were then washed and transferred to 24-well plates, individually. The growth of each spheroid was monitored with an inverted phase contrast microscope fitted with an ocular scale. Results are depicted in figures 9 and 10.
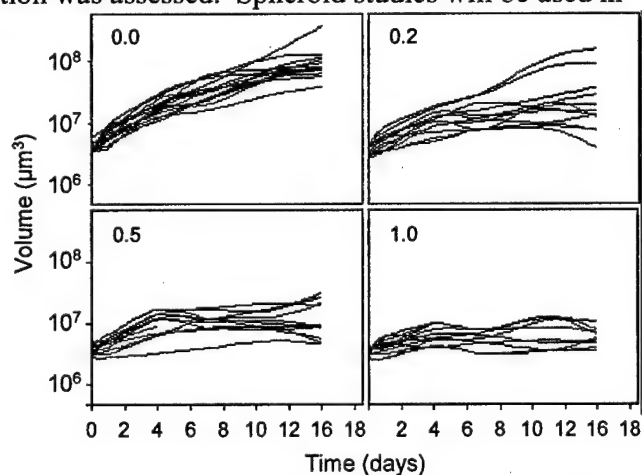

Fig. 9 Spheroid growth curves following exposure to different concentrations of [213]Bi irrelevant IgG (shown on the upper left corner of each panel, in MBq/ml). Each curve depicts the growth history of an individual spheroid.
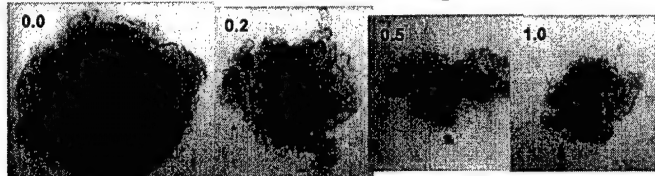

Fig. 10 Light microscope images of spheroids after 11 days of growth, following incubation with [213]Bi IgG (MBq/ml in upper left corner,)

It is important to note that the spheroid studies described above were performed using an irrelevant antibody, analogous studies using [213]Bi-labeled-7.16.4 are currently in progress. Such work will complement the upcoming *in vivo* studies by providing an *in vitro* model that may be used to support dosimetric modeling.

Modeling/Dosimetry Studies

Preliminary modeling/dosimetry calculations have been performed to evaluate the feasibility of using a potentially cross-reactive antibody to target metastatic disease with a short-lived alpha-particle emitter. Modeling is performed by using a multicompartmental model to solve the macrodistribution of antibody and then providing the output of this lumped parameter model as boundary conditions for a distributed parameter model that accounts for antibody diffusion and binding into a cluster of antigen positive tumor cells as well as a competing cluster of antigen-positive cross-reactive tumor cells. In turn, the results of this model are provided as input to a Monte Carlo model that performs a microdosimetric calculation to evaluate the specific energy distribution delivered to the tumor and normal cell populations. These data are then used to evaluate tumor control probability and to assess the likelihood of toxicity. The impact of unbound [213]Bi-labeled antibody on normal tissue that is in rapid access with IV injected antibody (e.g., marrow or liver parenchyma) is examined by considering the specific energy distribution of unbound antibody to a cluster of cells compared with specifically targeted antibody. All calculations are performed for intact antibody. The analyses are founded upon work previously performed by the PI (14-18). Figure 11 illustrates the

compartmental models used to simulate the macrodistribution of antibody and to provide boundary conditions for the distributed parameter cell model.
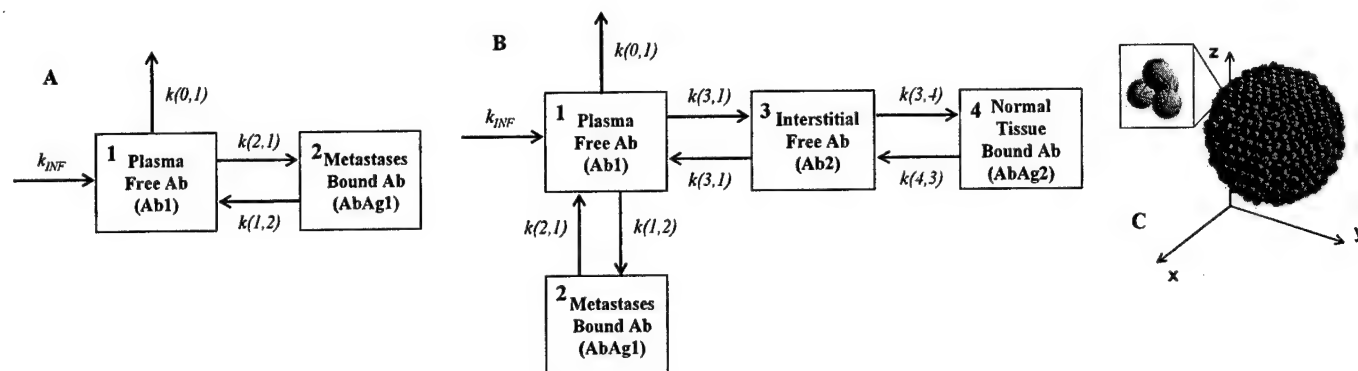

Fig. 11 The compartment models. <u>A)</u> The 2-compartment model represents a simple step of Ab binding to plasma-accessible tumor mets. Ab1, free Ab circulating in plasma; AbAg1, Ab bound to tumor met.antigen (Ag1); $k(2,1)$ and $k(1,2)$ are kinetic constants of Ab binding to and dissociation from Ag1 sites on tumor mets.; k_{INF} is the Ab infusion rate and $k(0,1)$ is the Ab clearance rate from plasma. <u>B)</u> The 4-compartment model is created by including a cross-reactive normal tissue compartment and its extracellular fluid (ECF) compartment. Ab extravasates from plasma to ECF before it can bind to cross-reactive normal tissue antigen (Ag2). $k(3,1)$ and $k(1,3)$ are extravasation and intravasation rates of the Ab while $k(3,4)$ and $k(4,3)$ are kinetic constants of Ab binding to and dissociation from the cross-reactive normal tissue. <u>C)</u> The spherical cell model used to represent either a pre-vascularized cluster of tumor cells or a vascularized cell cluster in a which the greatest distance of a particular cell from a capillary is no more than 100 μm. The same geometric model is used to represent normal, cross-reactive tissue. The sphere has an approximate radius of 100 μm, constructed by hexagonal close packing with 2146 cells of radius 7 μm.

The Monte Carlo (MC) code used to generate microdosimetric distributions of specific energy was validated against previously published results in which analytical solutions were obtained for tumor cells in suspension with alpha emissions on the surface of the cells or in the medium. Results comparing MC to analytical calculations are shown in figure 12.
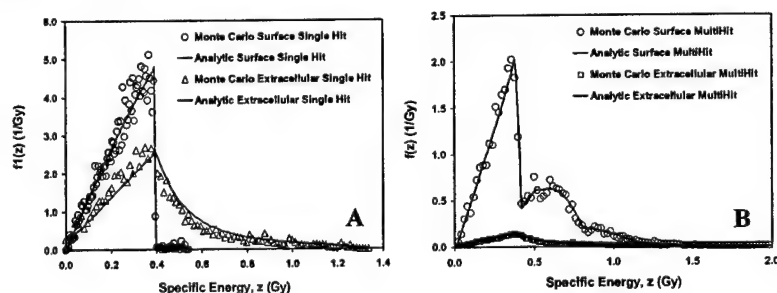
Fig. 12 <u>A)</u> The three dimensional Monte Carlo calculations of single hit distribution of ^{213}Bi on the cell surface (open circle) or in the extracellular space (open triangle) as compared to distributions obtained with geometrical analysis (lines) (Roeske paper). <u>B)</u> Monte Carlo calculations of multi-hit distribution of ^{213}Bi on cell surface (16 hits, open circle) and in extracellular space (64 hits, open square) as compared to distributions obtained by convolution of the single hit distribution (lines).

The results shown above demonstrate that the Monte Carlo model used in the microdosimetry calculations yields results consistent with those obtained by analytical calculation (solid lines in 12 A and 12 B). Macroscopic and microscopic antibody kinetics are depicted in figure 13 for different tumor burdens. The impact of tumor burden on plasma and extracellular fluid kinetics is illustrated in A, C and E. Penetration of antibody into spherical cell clusters is shown in panels B, D and F. Parameter values for these calculations were obtained from references (17;18).
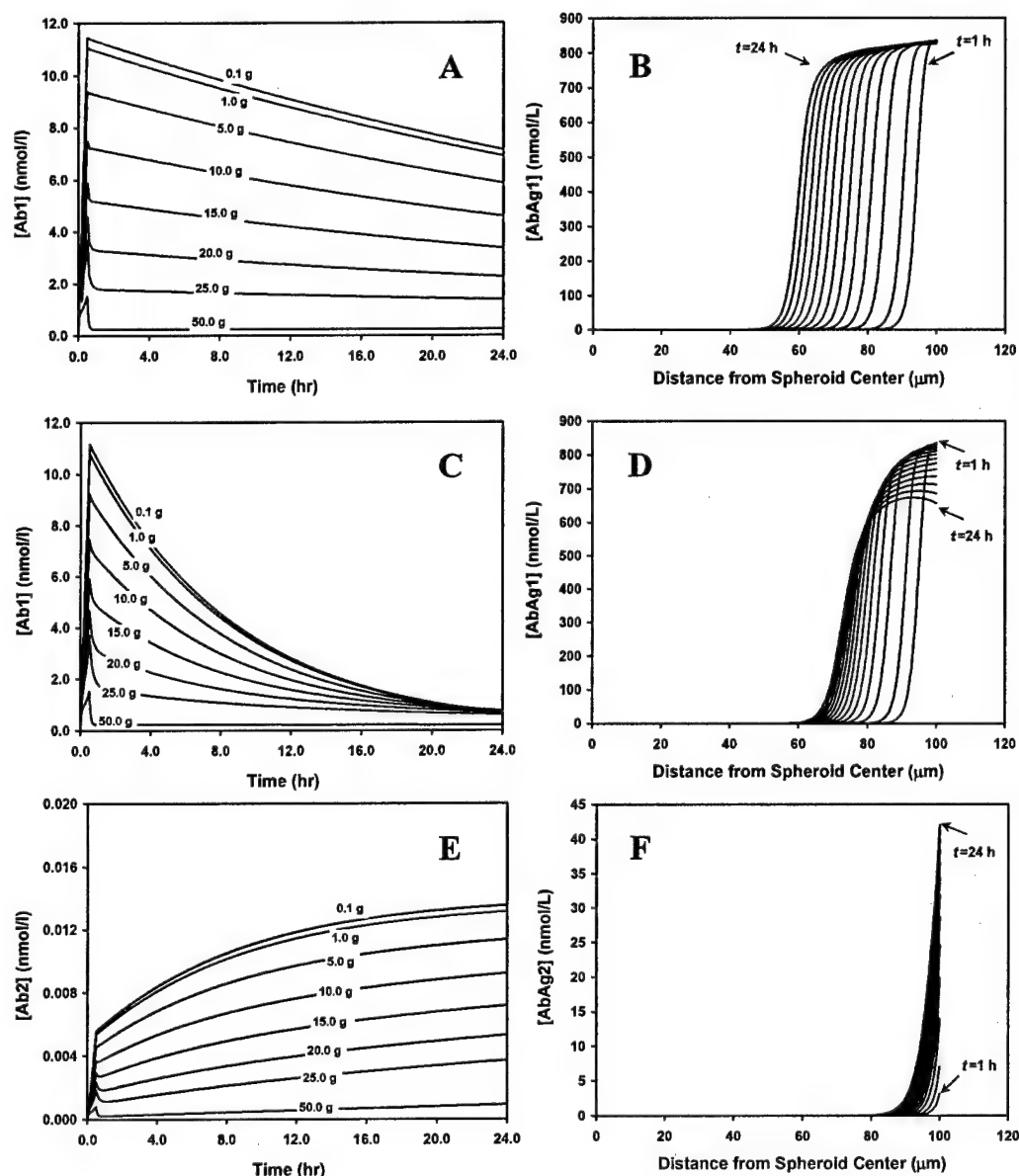

Fig. 13 Kinetics of Ab plasma clearance, diffusion and saturable binding in the compartmental and distributed parameter (i.e., spherical) models. *Two compartment model.* A) Ab 24hr plasma clearance after a half hour infusion of 43.8 nmol (6.6 mg) antibody with tumor burden ranging from 0.1g to 50g. B) Ab 24hr diffusion in a spherical tumor of radius 100 μm with tumor burden 1 g considering saturable binding and using the kinetis shown in A to give the concentration of Ab at the spheroid surface as a function f time. *Four compartment model.* C) Kinetics of Ab plasma clearance as in A while including a 20 g cross-reactive normal tissue compartment. Conservatively, the Ag density of the cross-reactive tissue is set the same as tumor. D) Antibody diffusion in a spherical tumor of radius 100 μm using parameters in C with 1 g tumor burden. E) Corresponding kinetics of free Ab in the extracellular fluid compartment of cross-reactive tissue. F) Diffusion of Ab in a spherical cross-reactive normal tissue within 24 hr using the same parameters as in D.

Comparing the first row (A and B) of simulations, above, with the second row (C and D), the results demonstrate that cross-reactive tissue will increase the clearance of antibody from plasma (as shown in C) and reduce the penetration of antibody into tumor clusters (note both cross reactive tissue and tumor were assumed to have the same target receptor expression). The last row of simulations shows that the added step of extravasation into normal organ ECF (E) yields a substantially reduced cross-reactive tissue penetration (F). The quantity of interest, however, in terms of tumor efficacy and normal tissue toxicity is absorbed dose. This is obtained by first considering the radioactivity concentration. In figure 14, kinetics of Ab penetration into tumor and cross-reactive normal tissue cell clusters are used to obtain the radioactivity concentration of ^{213}Bi. A comparison is made with ^{211}At, an alpha-emitter that has also been administered to humans for targeted therapy (19-22), and which has a 7.2 h half-life.
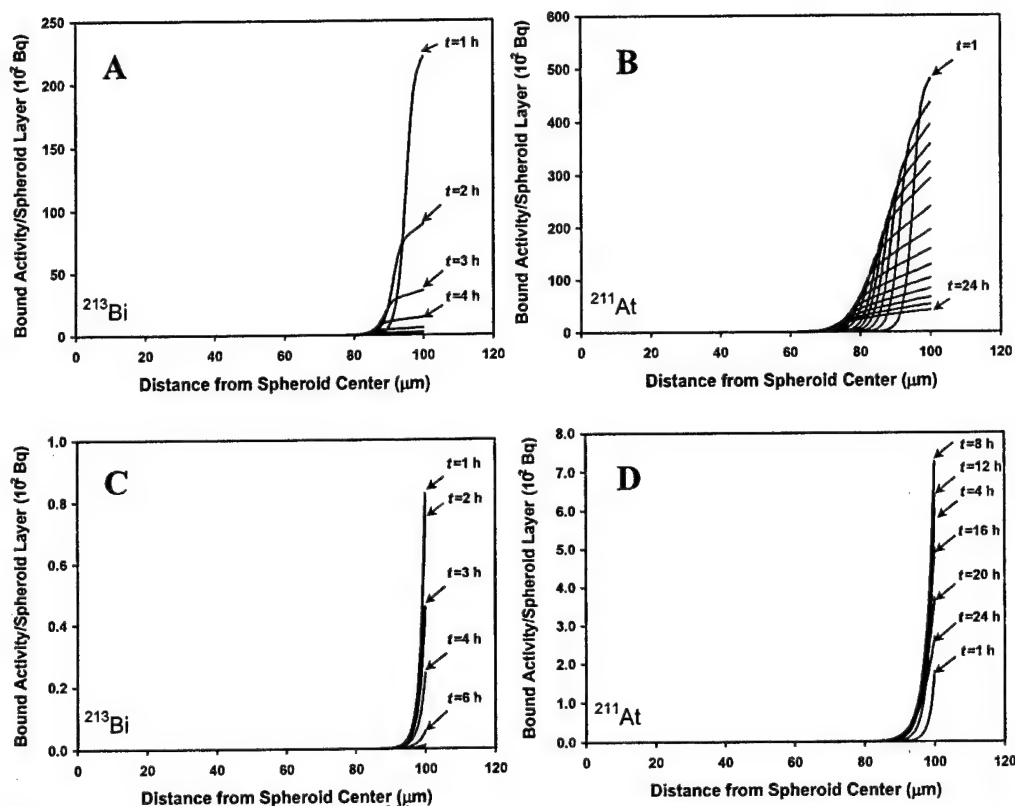
Fig. 14 Radioactivity of alpha emitter ^{213}Bi and ^{211}At labeled antibody (total injected activity 2.22×10^3 MBq; 60 mCi) in a spherical tumor/normal tissue cluster of 100 μm radius with the same diffusion kinetics as in Figure 13D and 13F. A) ^{213}Bi (half life=45.6min) and B) ^{211}At activity (half life=7.2hr) from cell bound antibody in plasma accessible tumor metastases. C) ^{213}Bi and D) ^{211}At activity from cell bound antibody in cross-reactive normal tissue on the extravascular side of basement membrane.

The first row of results shows that ^{211}At yields a 2.4-fold greater activity concentration at the surface of the cluster than does ^{213}Bi. As expected, the ^{211}At activity within the cluster persists longer and therefore penetrates deeper than that of ^{213}Bi (B vs A). In terms of radioactivity delivered to a tumor cell cluster, therefore, ^{211}At provides an advantage over ^{213}Bi. Panels C and D examine the difference between these two short-lived alpha-emitters in terms of potential toxicity, as reflected by radioactivity kinetics, to normal cross-reactive tissue. Comparing panel C with D, the maximum normal cross-reactive tissue for ^{211}At is 8- to 9-fold greater than for ^{213}Bi. The surface maximum is reached 8 h after injection and the activity penetration is slightly deeper than for ^{213}Bi. Taken together, these results, suggest that the toxicity profile of ^{211}At would negate its advantages in terms of tumor targeting. A proper comparision, however, requires absorbed dose estimation and the introduction of radiobiologic considerations such as tumor control probability. Figure 15 depicts the spatial distribution of energy deposition per cell for different source configurations within the tumor and also for cross reactive normal tissue. A comparison is made to ^{211}At.
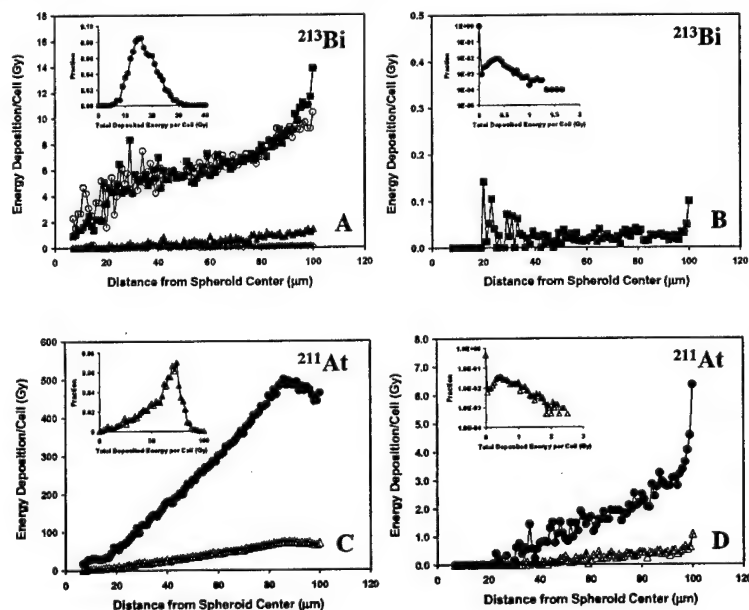

Fig. 15 Absorbed doses per cell at progressively deeper layers of the spherical tumor resulting from the kinetics and distribution of radioactivity in Figure 14. Small figures are the frequency distribution (expressed as fraction of cells) of total absorbed dose per cell. A) Absorbed doses per cell from ^{213}Bi, separately showing the four different sources of activity: cell-associated: 50% surface bound Ab (open circle), 50% internalized Ab (closed square), intercellular spaces (open diamond), external spaces of spheroid (closed triangle). B) Spatial distribution of total absorbed dose per cell from ^{213}Bi in normal, cross-reactive tissue. C) Spatial distribution of total absorbed dose per cell in tumor with total injection of 2.22×10^3 MBq (closed circle) and 3.33×10^2 MBq (open triangle) ^{211}At respectively. Small figure is the absorbed dose distribution for injection of 3.33×10^2 MBq ^{211}At, which results in similar tumor control probability (TCP, 85%-90%) for a tumor of radius 100 μm as that from injection of 2.22×10^3 MBq ^{213}Bi. D) Spatial distribution of total absorbed dose per cell in normal, cross-reactive tissue with total injection of 2.22×10^3 MBq (closed circle) and 3.33×10^2 MBq (open triangle) ^{211}At.

The results depicted above provide substantial insight into the targeting of metastatic tumor cells and the potential toxicity of normal organs. In panel A, we can see that, given the 80 μm range of ^{213}Bi alphas, the energy deposited per cell is insensitive to the exact position of the decay (surface vs cytosolic), also, since the tumor cells are assumed close-packed the contribution from decays within the interstitial space of the cluster is negligible. Of greater interest, however, is the observation that the contribution from non-specific decays, outside the cluster, is 10- to 12-fold lower than that received if the antibody is on the surface or within the cytosol. This result is consistent with previous observations/calculations (23;24); it corresponds to the situation of targeting tumor cell clusters in the liver or marrow space when the antibody is minimally cross-reactive with these tissues. The result demonstrates that freely circulating antibody will irradiate these rapidly accessible organ spaces substantially less than tumor cells contained within them. The inset graph of panel A depicts the fraction of cells making up the tumor spheroid that receive a particular absorbed dose. The plot shows that almost all cells within the cluster receive an absorbed dose between 10 and 30 Gy; no cells receive zero dose. The maximum dose from decays outside the spheroid (solid triangles), in contrast is approximately 1Gy, substantially lower than the minimum dose received by cells making up the cluster (including cells in the interior of the cluster). Panel B depicts the absorbed dose profile across a normal cross-reactive tissue that is only accessible after the antibody has extravasated across normal organ vasculature. The peak in energy deposition per cell just after 20 μm from the cluster center reflects the Bragg peak, a characteristic increase in the energy deposition near the end of an alpha-track that is associated with a rapid increase in linear energy transfer as the alpha slows down. This is not seen as clearly in panel A because, due to penetration it is spread out over a longer radial dimension. The dose-range of irradiated cells in this case is 10 to 20-fold lower than that obtained in panel A. The inset shows that the majority of cells receive no absorbed dose. Panels C and D show the results for ^{211}At. Panel C shows the dose profile when the administered activities are matched and also for an administered activity of ^{211}At that matches the tumor control probability (TCP) obtained from panel A. TCP is obtained by convolving the absorbed dose profile across the spheroid with a surviving fraction curve. The TCP comparison is made to account for the difference in total decays per unit administered activity of ^{211}At vs. ^{213}Bi; because of it's longer half-life there are more ^{211}At decays per unit activity than ^{213}Bi decays. The ^{211}At dose profiles peak at 10 to 20 μm from the cluster surface (90 to 80 μm from center). This is consistent with the greater penetration of ^{211}At (due to its longer half-life) and represents a "charged particle equilibrium" effect, wherein cells at the surface are subject to less radiation than those further inside because they are only irradiated from one side. It is not observed, as clearly, for the ^{213}Bi curve because the energy deposition is lower and the number of histories executed by MC were not increased in these prelim. studies to account for this. As shown by the inset plot, the dose to to tumor cells within the cluster is distributed over a wider range for ^{211}At, than that obtained with ^{213}Bi; the majority of cells in the cluster received a dose in excess of 50 Gy. The dose profile to normal cross-reactive tissue shown in panel D at an equi-TCP administered activity is approx. 10-fold greater than that observed with ^{213}Bi. The inset plot also shows that a smaller fraction of the cells in normal cross-reactive tissue receive a dose of zero. The interaction between tumor burden, antibody administered and the size of the metastases on tumor control and normal organ toxicity is examined in figure 16.
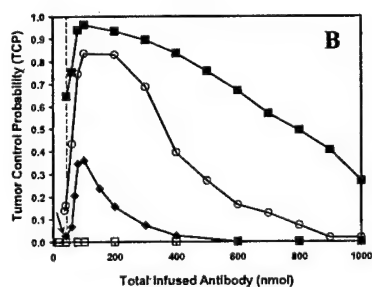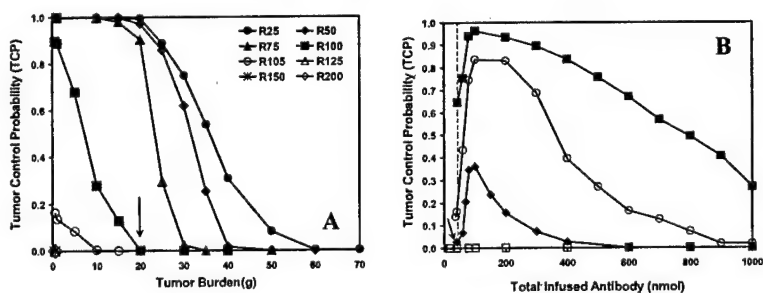

Fig. 16 A) Tumor control probability (TCP) obtained with 2.22x10³ MBq (60 mCi) ^{213}Bi on 43.8 nmol (6.6 mg) antibody) for different tumor metastases burdens (0.5 g to 70 g) distributed as foci of disease with radii ranging from 25 μm to 200 μm with the presence of 20 g cross-reactive normal tissue. B) Effects of total infused antibody and activity on tumor control probability (20g burden as R100). Total injected activity is 1.48x10³ MBq (open square), 2.22 x10³ MBq (closed diamond), 2.96 x10³ MBq (open circle) and 3.52 x10³ MBq (= 95 mCi; closed square). Total antibody amount was varied from 1000 nmole (150 mg) to injected activity divided by the maximum specific activity 8.03 x10⁷ Bq/nmol. Arrow indicates the same therapeutic condition as the arrow in A.

Panel A shows that for rapidly accessible tumors that are 75 μm in radius or less, tumor burdens of up to 15 g may be effectively treated. If the typical metastasis size is100 μm in radius, then the control probability is approximately 90% for microscopic disease, under the treatment described in the figure legend. This rapidly drops to zero as the tumor burden increases. As shown in panel B, however, increasing the amount of antibody, even if the administered activity is kept at 60 mCi, increases the TCP to 35%. Increasing both administered activity and antibody amount can yield TCP values greater than 90%. As the antibody administered is increased beyond an optimal level, however, the efficacy is reduced. The optimal level of Ab will

depend upon the tumor burden and in the case of panel B, above, corresponds to that which will saturate Ag sites on 20g of tumor cells. In all simulations depicted above, the 80 to 90% of the cells making up a 10 to 20 g cross-reactive normal tissue are expected to survive, whether this corresponds to prohibitive toxicity will depend upon the normal organ and the specific population of cells that are affected.

The theoretical studies presented in this section are preliminary and were intended primarily to examine targeting of pre-vascularized tissue. By adjusting the capillary transport parameters in the cross-reactive tissue model, the efficacy of targeting tumor tissue mets that are vascularized can be examined. Also the impact of Ag expression on rapidly accessible normal organs such as the marrow and liver can be examined by performing the simulations with a lower expression of Ag sites or with lower binding affinity for the Ab. The studies are included primarily to highlight the analytical approaches that will be used to evaluate data obtained from the ucoming animal studies.

Reference List

1 Guy CT, Webster MA, Schaller M, Parsons TJ, Cardiff RD, Muller WJ. Expression of the Neu Protooncogene in the Mammary Epithelium of Transgenic Mice Induces Metastatic Disease. *Proceedings of the National Academy of Sciences of the United States of America.* 1992; 89(22):10578-10582.

2 Guy CT, Webster MA, Schaller M, Parsons TJ, Cardiff RD, Muller WJ. Expression of the neu protooncogene in the mammary epithelium of transgenic mice induces metastatic disease. *Proc Natl Acad Sci U S A.* 1992; 89(22):10578-10582.

3 Wolpoe ME, Lutz ER, Ercolini AM, Murata S, Ivie SE, Garrett ES et al. HER-2/neu-specific monoclonal antibodies collaborate with HER-2/neu-targeted granulocyte macrophage colony-stimulating factor secreting whole cell vaccination to augment CD8(+) T cell effector function and tumor-free survival in Her-2/neu-transgenic mice. *Journal of Immunology.* 2003; 171(4):2161-2169.

4 Reilly RT, Machiels JPH, Emens LA, Ercolini AM, Okoye FI, Lei RY et al. The collaboration of both humoral and cellular HER-2/neu-targeted immune responses is required for the complete eradication of HER-2/neu-expressing tumors. *Cancer Research.* 2001; 61(3):880-883.

5 Reilly RT, Gottlieb MBC, Ercolini AM, Machiels JPH, Kane CE, Okoye FI et al. HER-2/neu is a tumor rejection target in tolerized HER-2/neu transgenic mice. *Cancer Research.* 2000; 60(13):3569-3576.

6 Arguello F, Baggs RB, Frantz CN. A murine model of experimental metastasis to bone and bone marrow. *Cancer Res.* 1988; 48(23):6876-6881.

7 Song H, Shahverdi K, Reilly RT, Yoder B, Fox J, Qi Y et al. A bone metastasis model for absorbed dose-response studies in targeted radionuclide therapy. *Proceedings 1st International Radiopharmaceutical Therapy and Dosimetry Symposium.* 2004; in press.

8 Berger F, Lee YP, Loening AM, Chatziioannou A, Freedland SJ, Leahy R et al. Whole-body skeletal imaging in mice utilizing microPET: optimization of reproducibility and applications in animal models of bone disease. *Eur J Nucl Med Mol Imaging.* 2002; 29(9):1225-1236.

9 Goddu SM, Howell RW, Rao DV. Cellular dosimetry: absorbed fractions for monoenergetic electron and alpha particle sources and S-values for radionuclides uniformly distributed in different cell compartments. *J Nucl Med.* 1994; 35(2):303-316.

10 Vandenbulcke K, De Vos F, Offner F, Philippe J, Apostolidis C, Molinet R et al. In vitro evaluation of 213Bi-rituximab versus external gamma irradiation for the treatment of B-CLL patients: relative biological efficacy with respect to apoptosis induction and chromosomal damage. *Eur J Nucl Med Mol Imaging.* 2003; 30(10):1357-1364.

11 Enmon R, Yang WH, Ballangrud AM, Solit DB, Heller G, Rosen N et al. Combination treatment with 17-N-allylamino-17-demethoxy geldanamycin and acute irradiation produces supra-additive growth suppression in human prostate carcinoma spheroids. *Cancer Res.* 2003; 63(23):8393-8399.

12 Ballangrud AM, Yang WH, Dnistrian A, Lampen NM, Sgouros G. Growth and characterization of LNCaP prostate cancer cell spheroids. *Clin Cancer Res.* 1999; 5(10 Suppl):3171s-3176s.

13 Yuhas JM, Li AP, Martinez AO, Ladman AJ. A simplified method for production and growth of multicellular tumor spheroids. *Cancer Res.* 1977; 37(10):3639-43.

14 Sgouros G, O'Donoghue JA, Larson SM, Macapinlac H, Larson JJ, Kemeny N. Mathematical model of 5-[125I]iodo-2'-deoxyuridine treatment: continuous infusion regimens for hepatic metastases. *Int J Radiat Oncol Biol Phys.* 1998; 41(5):1177-83.

15 Loh A, Sgouros G, O'Donoghue JA, Deland D, Puri D, Capitelli P et al. Pharmacokinetic model of iodine-131-G250 antibody in renal cell carcinoma patients. *J Nucl Med.* 1998; 39(3):484-9.

16 Willins JD, Sgouros G. Modeling Analysis of Platinum-195M for Targeting Individual Blood-Borne Cells in Adjuvant Radioimmunotherapy. *Journal of Nuclear Medicine.* 1995; 36(2):315-319.

17 Sgouros G, Graham MC, Divgi CR, Larson SM, Scheinberg DA. Modeling and dosimetry of monoclonal antibody M195 (anti-CD33) in acute myelogenous leukemia. *J Nucl Med.* 1993; 34(3):422-30.

18 Sgouros G. Plasmapheresis in radioimmunotherapy of micrometastases: a mathematical modeling and dosimetrical analysis [see comments]. *J Nucl Med.* 1992; 33(12):2167-79.

19 Zalutsky MR, Cokgor I, Akabani G, Friedman HS, Coleman RE, Friedman AH et al. Phase I trial of alpha-particle-emitting astatine-211 labeled chimeric anti-tenascin antibody in recurrent malignant glioma patients. *Proceedings of The American Association for Cancer Research.* 2000; 41:544.

20 Zalutsky MR, Vaidyanathan G. Astatine-211-Labeled Radiotherapeutics: An Emerging Approach to Targeted Alpha-Particle Radiotherapy. *Curr Pharm Des.* 2000; 6(14):1433-1455.

21 Akabani G, Cokgor I, Coleman RE, Gonzalez Trotter D, Wong TZ, Friedman HS et al. Dosimetry and dose-response relationships in newly diagnosed patients with malignant gliomas treated with iodine-131-labeled anti-tenascin monoclonal antibody 81C6 therapy. *Int J Radiat Oncol Biol Phys.* 2000; 46(4):947-958.

22 Zalutsky MR, Akabani G, Cokgor I, Friedman HS, Coleman RE, Friedman AH et al. Astatine-211 labeled chimeric anti-tenascin antibody: Phase I trial in brain tumor resection cavity patients. *European Journal of Nuclear Medicine.* 1999; 26(9):PS651.

23 Humm JL, Chin LM. A model of cell inactivation by alpha-particle internal emitters. *Radiat Res.* 1993; 134(2):143-50.

24 Humm JL. Dosimetric aspects of radiolabeled antibodies for tumor therapy. *J Nucl Med.* 1986; 27(9):1490-7.

Pharmacokinetics and Biodistribution of [86]Y-Trastuzumab for [90]Y Dosimetry in an Ovarian Carcinoma Model: Correlative MicroPET and MRI

Stig Palm, PhD[1]; Richard M. Enmon, Jr., PhD[1]; Cornelia Matei, SB[1]; Katherine S. Kolbert, MS[1];
Su Xu, PhD[1]; Pat B. Zanzonico, PhD[1]; Ronald L. Finn, PhD[1]; Jason A. Koutcher, MD, PhD[1];
Steven M. Larson, MD[2]; and George Sgouros, PhD[1,3]

[1]Department of Medical Physics, Memorial Sloan-Kettering Cancer Center, New York, New York; [2]Department of Radiology, Memorial Sloan-Kettering Cancer Center, New York, New York; and [3]Department of Radiology, Johns Hopkins University School of Medicine, Baltimore, Maryland

Preclinical biodistribution and pharmacokinetics of investigational radiopharmaceuticals are typically obtained by longitudinal animal studies. These have required the sacrifice of multiple animals at each time point. Advances in small-animal imaging have made it possible to evaluate the biodistribution of radiopharmaceuticals across time in individual animals, in vivo. MicroPET and MRI-based preclinical biodistribution and localization data were obtained and used to assess the therapeutic potential of ^{90}Y-trastuzumab monoclonal antibody (mAb) (anti-HER2/neu) against ovarian carcinoma. **Methods:** Female nude mice were inoculated intraperitoneally with $5 \cdot 10^6$ ovarian carcinoma cells (SKOV3). Fourteen days after inoculation, 12–18 MBq [86]Y-labeled trastuzumab mAb was injected intraperitoneally. Tumor-free mice, injected with [86]Y-trastuzumab, and tumor-bearing mice injected with labeled, irrelevant mAb or [86]Y-trastuzumab + 100-fold excess unlabeled trastuzumab were used as controls. Eight microPET studies per animal were collected over 72 h. Standard and background images were collected for calibration. MicroPET images were registered with MR images acquired on a 1.5-T whole-body MR scanner. For selected time points, 4.7-T small-animal MR images were also obtained. Images were analyzed and registered using software developed in-house. At completion of imaging, suspected tumor lesions were dissected for histopathologic confirmation. Blood, excised normal organs, and tumor nodules were measured by γ-counting. Tissue uptake was expressed relative to the blood concentration (percentage of injected activity per gram of tissue [%IA/g]/%IA/g blood). [86]Y-Trastuzumab pharmacokinetics were used to perform ^{90}Y-trastuzumab dosimetry. **Results:** Intraperitoneal injection of mAb led to rapid blood-pool uptake (5–9 h) followed by tumor localization (26–32 h), as confirmed by registered MR images. Tumor uptake was greatest for [86]Y-trastuzumab (7 ± 1); excess unlabeled trastuzumab yielded a 70% reduction. Tumor uptake for the irrelevant mAb

was 0.4 ± 0.1. The concentration in normal organs relative to blood ranged from 0 to 1.4 across all studies, with maximum uptake in spleen. The absorbed dose to the kidneys was 0.31 Gy/MBq ^{90}Y-trastuzumab. The liver received 0.48 Gy/MBq, and the spleen received 0.56 Gy/MBq. Absorbed dose to tumors varied from 0.10 Gy/MBq for radius = 0.1 mm to 3.7 Gy/MBq for radius = 5 mm. **Conclusion:** For all injected compounds, the relative microPET image intensity of the tumor matched the subsequently determined [86]Y uptake. Coregistration with MR images confirmed the position of [86]Y uptake relative to various organs. Radiolabeled trastuzumab mAb was shown to localize to sites of disease with minimal normal organ uptake. Dosimetry calculations showed a strong dependence on tumor size. These results demonstrate the usefulness of combined microPET and MRI for the evaluation of novel therapeutics.

Key Words: microPET; trastuzumab; [86]Y; ovarian carcinoma; pharmacokinetics

Pharmacokinetics and biodistribution of radiopharmaceuticals in preclinical animal studies have generally been obtained by extraction of selected organs and scintillation counting for radioactivity at different times after injection. This approach requires the sacrifice of multiple animals at each time point, precludes the ability to monitor biodistribution in individual animals, and is partially susceptible to selection bias because unexpected accumulation of radioactivity in tissue not collected for scintillation counting will be missed. The availability of small-animal imaging instrumentation and positron-emitting analogs of therapeutic radionuclides (e.g., [86]Y and [124]I for ^{90}Y and ^{131}I, respectively) has made it possible to obtain preclinical pharmacokinetics noninvasively using imaging-based methods. The advantages of such an approach include the ability to monitor kinetics in individual animals over time and the ability to

obtain whole-body images of biodistribution, thereby reducing the likelihood that areas of unexpected radiopharmaceutical accumulation will be missed. Together, these increase the statistical power of each measurement, reducing total animal requirements. The disadvantages include a reduction in quantitative accuracy and difficulty in placing the radioactivity distribution in the proper anatomic context. The latter difficulty arises because of resolution limitations and because images of radionuclide distribution do not typically provide detailed anatomic information.

In this work, the positron-emitting radionuclide ^{86}Y, in conjunction with small-animal PET (microPET) imaging, is used to evaluate pharmacokinetics and dosimetry of ^{90}Y-trastuzumab in a disseminated ovarian carcinoma model. MRI, in conjunction with image registration, was used to correlate the radiolabeled monoclonal antibody (mAb) distribution with anatomy. At the end of imaging, the animals were killed and conventional organ biodistribution information was obtained by γ-counting. The combination of these approaches satisfactorily addressed the issues of anatomic localization and quantitative accuracy.

^{86}Y has a 14.7-h half-life ($t_{1/2}$) and decays by positron emission. The relatively long half-life allows the acquisition of PET images 2–3 d after injection. Being isotopes of the same element, ^{86}Y is chemically identical to ^{90}Y, a pure β-particle–emitting radionuclide that is under investigation for use in targeted radionuclide therapy (1,2). A drawback of using ^{90}Y is that the lack of emitted photons makes it difficult to study the biodistribution of the injected compound. To overcome this obstacle, alternative nuclides have been used. The most commonly used is ^{111}In; however, with PET cameras becoming more available, the use of the positron emitter ^{86}Y has been suggested as a better substitute. A nuclide of the same element is expected to behave chemically identically and thus serve better than a nuclide of another element. Comparisons between these 2 ^{90}Y substitutes—that is, ^{111}In and ^{86}Y—have recently been made (3,4).

The anti-HER2/neu mAb, trastuzumab, has demonstrated efficacy in the treatment of cancer patients whose disease exhibits high levels of HER2/neu expression (5,6). In several studies, trastuzumab has been shown to potentiate chemotherapy (7,8). The possibility of using radiolabeled anti-HER2/neu mAbs for cancer therapy has been previously considered (9).

MATERIALS AND METHODS

Cell Culture and Tumor Inoculation

The human ovarian carcinoma cell line SKOV3-NMP2 was provided by Dr. Paul Borchardt (Memorial Sloan-Kettering Cancer Center [MSKCC]). Subclone NMP2 was originally created at the University of Texas M.D. Anderson Cancer Center by passage of the line through nude mice and selected for this study because of enhanced tumorigenicity (10). Stock T-flask cultures were propagated at 37°C, in 95% relative humidity, and in 5% CO$_2$ in RPMI 1640 medium (Invitrogen) supplemented with 10% fetal calf serum (Sigma), 100 units/mL penicillin, and 100 mg/mL streptomy-

cin (Gemini Bio-Products). Cell concentrations were determined by counting trypsinized cells with a hemocytometer. Tumor inoculum was prepared as a single-cell suspension at $1 \cdot 10^7$ cells/mL in complete RPMI 1640 medium. Each 4- to 6-wk-old female BALB/c nude mouse (Taconic) received 0.5 mL inoculum ($5 \cdot 10^6$ cells) administered by intraperitoneal injection. Animals receiving 0.5 mL of media alone served as negative controls.

Mice were housed in filter top cages and provided with sterile food and water. Animals were maintained according to the regulations of the Research Animal Resource Center at MSKCC, and animal protocols were approved by the Institutional Animal Care and Use Committee.

Preparation of Radioimmunoconjugate

mAb–chelate conjugates were provided as gifts: humanized anti-HER-2, trastuzumab (Herceptin; Genentech, Inc.), was provided by Dr. Paul Borchardt and prepared according to Borchardt et al. (11); humanized anti-CD33, HuM195 (Protein Design Labs, Inc.), was provided by Dr. Michael McDevitt (MSKCC) and prepared according to McDevitt et al. (12). A backbone-substituted derivative of diethylenetriamine pentaacetic acid (DTPA), 2-(4-isothiocyanatobenzyl)DTPA (SCN-CHX-A-DTPA), served as the chelate in all conjugation reactions. mAb conjugate was typically supplied at 7–10 mg/mL.

^{86}Y was produced by irradiating isotope-enriched ^{86}SrCO$_3$ (97.02% ^{86}Sr) with 15-MeV protons in the cyclotron facility (model CS-15; Cyclotron Corp.) of MSKCC (13). The ^{86}Y was dissolved in 0.2–0.4 mL of 50 mmol/L HCl, generating ^{86}YCl$_3$. The radioactivity was measured with a dose calibrator (model CRC-15R; Capintec) and a NaI(Tl) γ-counter (model 5003, Cobra II; Packard).

Radiolabeling protocols were based on those developed in Nikula et al. (14,15). These references similarly outline methods for assessing reaction efficiency using instant thin-layer chromatography (ITLC) and for evaluating final immunoreactivity of the product. Briefly, 0.2–0.3 mL of 3 mol/L ammonium acetate was added to the ^{86}YCl$_3$ solution to adjust to pH ~5.5. Approximately 200 μg of mAb conjugate were added and the reaction was allowed to proceed at 25°C for 30 min. The reaction was quenched by the addition of 0.040 mL of 10 mmol/L ethylenediaminetetraacetic acid. Radiolabeled mAb was purified from unbound isotope by size-exclusion chromatography using a 10-DG size-exclusion column (Bio-Rad Laboratories, Inc.). Minimum reaction efficiency was 70% as determined by ITLC. The radioactivity of the eluent was determined as previously described. Specific activity varied from 0.7 to 1.0 MBq/μg. Immunoreactivity as determined by acid wash was >90%.

MicroPET Imaging

Two weeks after tumor inoculation, each mouse received 15 MBq (~20 μg) labeled mAb in 0.5 mL RPMI 1640 medium administered intraperitoneally. Mice receiving radiolabeled HuM195 prepared similarly or 15 MBq free ^{86}Y in 0.5 mL medium served as negative controls. A competitive control was created by adding an additional 2 mg unlabeled mAb to the injectate (excess cold control). For each experiment, a 20-mL glass scintillation vial filled with medium and containing 15 MBq ^{86}Y-trastuzumab was used as a standard. The microPET scanner used in these studies was not fitted with a transmission source; therefore, transmission studies were not collected for attenuation correction of the emission data.

Time-dependent distribution and localization of mAb were determined by 8 microPET imaging sessions over the course of 3 d. During each session a background scan and an image of the standard were also acquired. With the exception of the background, a minimum of $15 \cdot 10^6$ true counts per scan were collected to ensure adequate image quality. This required aquisition times of 2–5 min on day 0, 10–20 min on day 1, and 40 min on day 2 or 3 after injection. The mice were initially anesthetized using an isoflurane (Forane; Baxter) loaded vaporizer (Vetequip) attached to an incubation chamber. The mice were then placed on the imaging table and were kept anesthetized during the image acquisition by switching the vaporizer to a fitted nose cone.

MRI

On day 5 or 6 after injection, each mouse was imaged on a 1.5-T whole-body MR scanner (Signa; General Electric Medical Systems) to provide anatomic images for registration with PET scans. Five or 6 mice were anesthetized using 106 mg/kg ketamine and 5.5 mg/kg acepromasine, placed in an in-house–fabricated mouse coil designed for imaging up to 13 mice simultaneously (16), and imaged in a single 30- to 40-min session. Imaging parameters included a field of view of 8 × 8 mm, slice thickness of 1.5 mm, slice interval of 0.5 mm, imaging matrix of 512 × 512, a fast spin echo pulse sequence with a repetition interval (TR) of 4,500–11,000 ms, echo time (TE) arranged 96–102 ms, and 4 excitations per phase-encoding step. Selected mice were further imaged on a small-animal 4.7-T MR scanner (Omega; General Electric Medical Systems). A T2-weighted pulse sequence was also used on the 4.7-T scanner with a TR of 3,500 ms, TE of 40 ms, 1-mm-thick slice, imaging matrix of 256 × 256, and a 3-cm field of view.

Image Analysis and MicroPET Activity Quantitation

Image reconstruction was performed by filtered backprojection. In-house–developed software, MIAU (17) and 3-dimensional internal dosimetry (3D-ID) package (18), were used to quantitate reconstructed images and also for registration to MR studies. Whole-body clearance kinetics were obtained from the summed counts in each scan at each time point. Total counts were corrected for dead time and background. The decay-corrected total counts for the standard obtained in this manner varied by <2% over 72 h. Relative activity concentrations over the injection site, heart, and tumor were obtained by drawing regions of interests (ROIs). MicroPET quantitation can be influenced by the position of tissue relative to the central axis of the camera and also by the surrounding tissue, due to differential sensitivity and attenuation, respectively. Direct comparison of tumor to organ activity concentration was therefore not made; rather, only relative changes in the activity concentration in these tissues over time were evaluated. To minimize partial-volume effects arising because the activity containing volume (e.g., tumor nodules) is below the intrinsic resolution of the scanner, ROIs were consistently drawn to enclose a 30- to 40-μL volume.

Excised Organ Quantitation

Mice were killed on day 6 after injection by CO_2 intoxication for dissection. Blood was collected via cardiac puncture. Organ, muscle, and tumor tissues were washed in phosphate-buffered saline and weighed. The samples were then counted for photons in a γ-counter (model 5003, Cobra II; Packard). Two 100-μL aliquots of the 20-mL imaging standard were used for calibration of γ-counting results. Results are expressed as the radioactivity concentration in each organ divided by the concentration in blood.

Dosimetry

[86]Y-Trastuzumab kinetics and biodistribution were used to estimate absorbed doses for trastuzumab labeled with ^{90}Y, the therapeutically relevant radionuclide. Absorbed doses were estimated for the liver, kidneys, spleen, and tumor. A time–activity curve for blood was generated by determining the relative activity concentration from ROIs over the heart on repeated microPET images. The curve was then scaled to fit the activity concentration in collected blood at the time of dissection by extrapolating the monoexponential clearance phase of the curve. The activity concentration in liver, spleen, and kidneys was determined by γ-counting after dissection. The shape of the blood time–activity curve was used to construct a time–activity curve for each organ. The curve was scaled so that the activity concentration of the curve yielded the measured concentration at the time of dissection.

Tumor kinetics were obtained using the tumor ROI. Activity concentration in dissected tumor was fit to an extrapolated plateau in the time–activity curve. All curves were converted to represent physical-decay–corrected [86]Y-trastuzumab uptake (% injected activity per gram tissue, %IA/g). Assuming the same distribution for ^{90}Y-trastuzumab, the cumulated activity concentration (Ã/g) was calculated by integrating the decay-corrected uptake curves with the physical half-life of [90]Y:

$$\frac{\tilde{A}}{g} = \int_0^\infty A_0 \cdot \frac{f(t)}{100} \cdot e^{-\lambda \cdot t} dt, \qquad \text{Eq. 1}$$

where A_0 is the total amount of ^{90}Y-trastuzumab activity injected in the mouse (Bq), $f(t)$ is the time-dependent uptake of ^{90}Y-trastuzumab (%IA/g), and λ is the decay constant of [90]Y $(3.0038 \cdot 10^{-6} s^{-1})$.

Absorbed doses were calculated following the MIRD formalism (19). Absorbed fractions of electron energy emitted from a homogeneous distribution of ^{90}Y in spheres of various sizes (20) were used for tumor absorbed dose calculations. Recently published murine-specific S factors (21) were used to calculate self and cross-organ absorbed dose for liver, spleen, and kidneys. In the work cited, murine S factors were generated on the basis of the anatomic structure of an actual mouse as defined by noninvasive, high-resolution MRI. Using the previously developed 3D-ID package (18), organ contours were drawn and the resulting 3-dimensional organ volumes were convolved with individual radioisotope point kernels to calculate the S-factor values.

RESULTS

Tumor Take

The efficiency of tumor formation in this ovarian carcinoma model was 100% ($n = 23$). A consistent tumor distribution pattern was observed with histologically confirmed tumor nodules always appearing within 2–3 wk on the ventral side of the spleen (Fig. 1). Tumor was also frequently found dispersed within the mesentery with small (~1 mm), dense tumor nodules forming a "beads-on-a-string" configuration.

MicroPET Imaging

Time-sequential microPET images of coronal slices selected through the same plane (2 or 3 slices, ~1 mm, above

FIGURE 1. Dissected mouse. Arrow indicates location of small tumor nodules on spleen.

the bed) are shown in Figure 2. Images obtained using the specific mAb ($n = 8$) show high intensity at the injection site and subsequent accumulation of radioactivity in the circulation, as reflected by high cardiac signal intensity.

This first becomes visible within 3 h and is most intense at ~20 h after injection. Over this same time course tumor nodules become visible, first in the intestinal area and subsequently (e.g., by 30–40 h after injection) in the vicinity of the spleen. Tumor nodules were consistently visualized around the spleen in all animals. By 71 h, activity in the circulation is reduced and radioactivity persists at histopathologically confirmed tumor sites. In the 71-h image, the localization that is observed near the injection site corresponds to subcutaneous tumor nodules that occur as a result of the intraperitoneal tumor cell inoculation.

Corresponding coronal slices for several different control experiments are also shown on Figure 2. In mice injected with a 100-fold excess of unlabeled trastuzumab ($n = 3$), tumor localization was less apparent. In tumor-free mice ($n = 3$), the radioactivity distribution over time was similar to that of the tumor-bearing mice with the exception that the dominant signal intensity arose from activity in the circulation; accumulation at sites that would typically contain tumor nodules was not evident. The distribution pattern seen with the irrelevant, anti-CD33 mAb ($n = 6$) was similarly dominated by activity in the circulation.
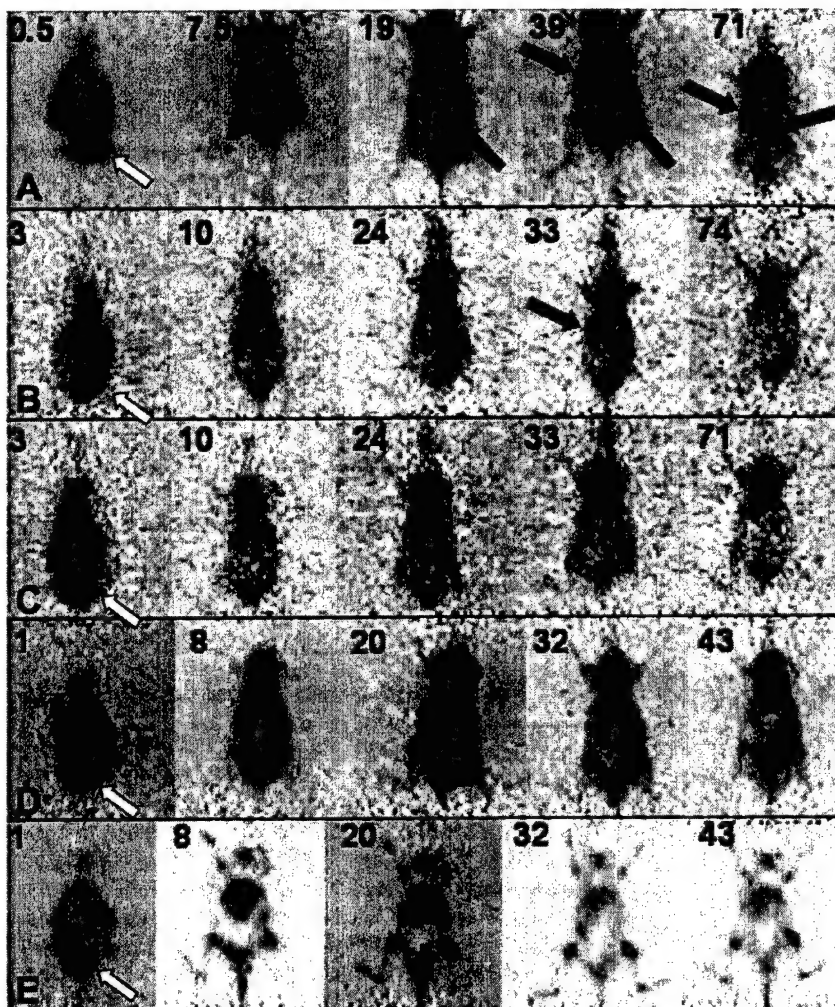

FIGURE 2. Longitudinal microPET coronal slice images of [86]Y-trastuzumab (A), excess unlabeled trastuzumab (B), [86]Y-trastuzumab on nontumor-bearing mice (C), [86]Y-HuM195 (D), and free [86]Y (E). Numbers in upper left corner of each panel indicate time after injection (in hours). Black arrows indicate mAb accumulation at confirmed tumor sites. White arrows indicate injection site.

Images obtained after the administration of free ^{86}Y (likely to be ^{86}Y-phosphate on injection; $n = 4$) showed, as expected, accumulation in bone. The whole skeleton was visualized in these studies, with a slightly higher uptake around the various joints. These studies were useful in ensuring that the pattern observed with the specific mAb was due to radiolabeled mAb localization rather than localization of free ^{86}Y, as might arise because of degradation of the chelated mAb. Such a pattern was only observed to a small extent, at 43 h after injection for the irrelevant control studies.

MRI

Figure 3, illustrates the typical tumor distribution observed in our model. In Fig. 3A, high-resolution transverse MR image slices obtained at 1.5 T are registered to corresponding micro-PET slices, providing anatomic context regarding the location of tumor nodules. The images in Fig. 3B depict multiple small (<1-mm diameter) tumor nodules associated with the spleen (left panel) and the mesentery (right panel).

Pharmacokinetics

Whole-body clearance was determined from the total counts in each image set. The specific mAb had the slowest clearance ($t_{1/2} = 160 \pm 10$ h [mean $\pm$ SE]), but not significantly different from that of the irrelevant HuM195 ($t_{1/2} = 150 \pm 50$ h) or free ^{86}Y ($t_{1/2} = 140 \pm 50$ h). Controls with an excess of unlabeled specific mAb had a more rapid whole-body clearance ($t_{1/2} = 90 \pm 20$ h), similar to that of specific mAb in nontumor-bearing mice ($t_{1/2} = 110 \pm 60$ h).

The group of mice receiving the specific mAb was evaluated for tumor and organ dosimetry. Initially, the activity concentration over the injection site decreased rapidly, reflecting redistribution in the circulation. This was followed by a slow uptake to a plateau level due to tumor at the trocar wound site (Fig. 4A). Blood kinetics showed a rapid uptake phase, followed by a slow clearance. Tumor had an essentially instantaneous uptake, slowly increasing to the stable maximum activity concentration at around 40 h after injection (Fig. 4B).
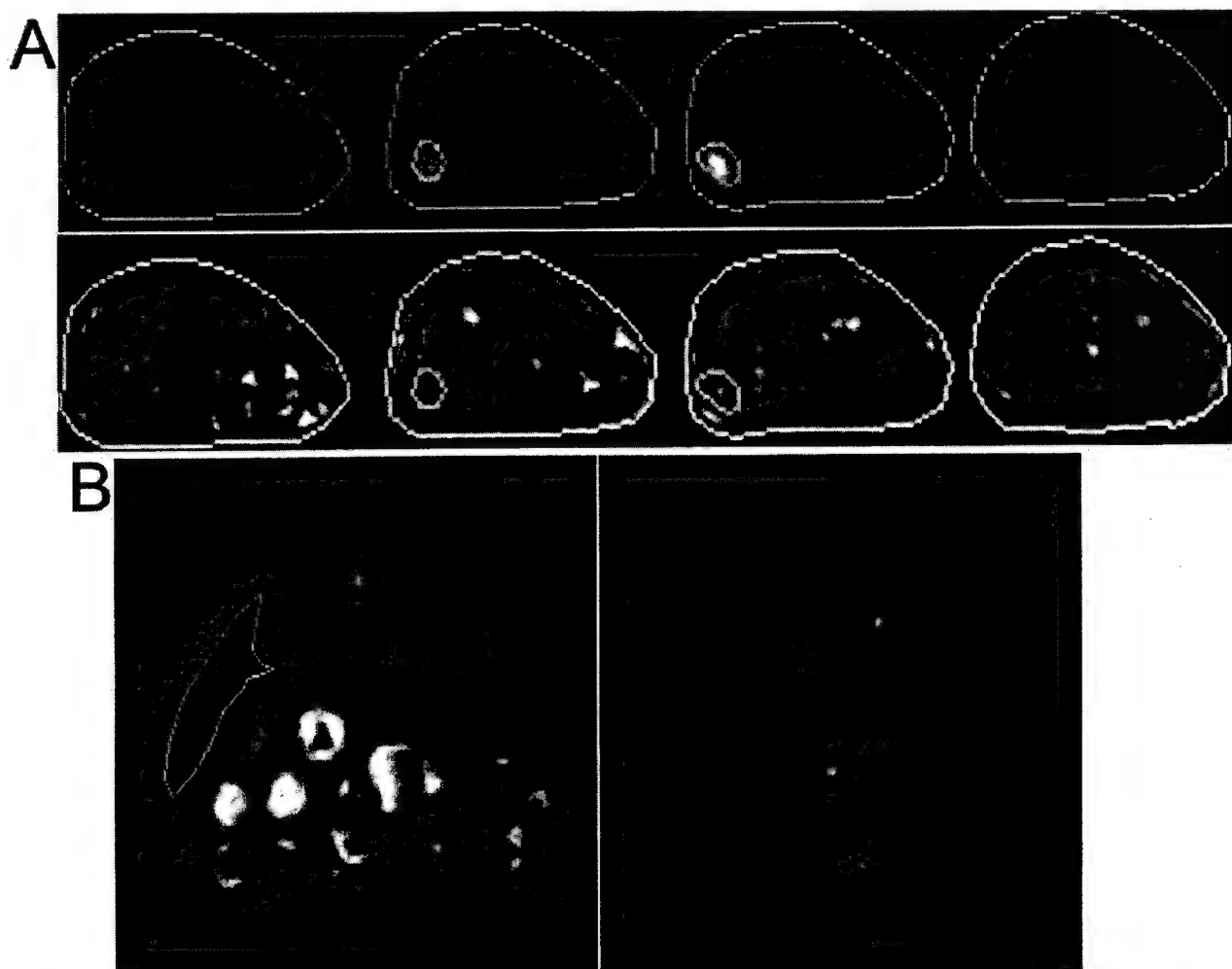

FIGURE 3. (A) High-resolution transverse MR image slices, registered to corresponding microPET slices. Contours depicting outer periphery of mouse and also collection of tumor nodules near spleen are shown. (B) Two transverse MR slices, obtained on small-animal (4.7 T) scanner, are shown. Two slices are taken at different transaxial positions. Slice on left is through spleen (yellow contour), kidneys (blue), and tumor nodules (orange). Slice on right is posterior to left slice and depicts multiple small tumor nodules in mesentery.
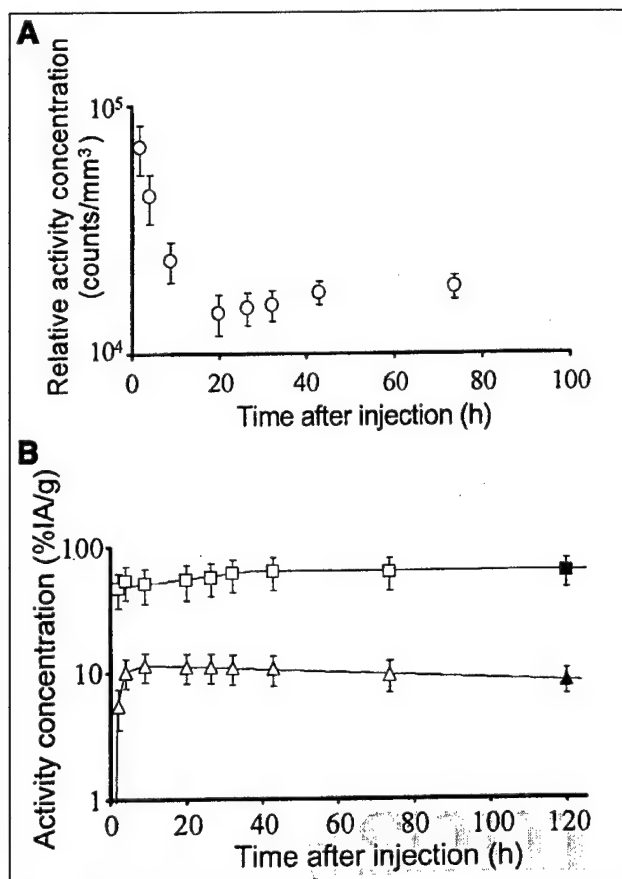
FIGURE 4. (A) Time–activity curve over injection site. Relative activity concentrations were determined by drawing ROIs on microPET image sets. Data are corrected for acquisition time, physical decay, and background. Error bars represent SE. (B) Time–activity curves for blood (triangles) and tumor (squares). Open symbols represent relative activity concentration (e.g., pharmacokinetics) derived from repeated microPET imaging. Activity concentrations (%IA/g) in dissected tissue (solid symbols) were used to quantitate image-based relative concentrations. Error bars represent combined standard uncertainty. Lines show fits used for cumulated activity calculations.

Biodistribution

The radioactivity distribution, obtained by well scintillation (γ) counting of excised tissues is shown in Figure 5. Uptake was represented as the organ-to-blood activity concentration ratio. The highest uptake, 7.4 ± 0.9 (mean $\pm$ SE), was found for [86]Y-trastuzumab specific mAb on tumor. When a 100-fold excess of unlabeled trastuzumab mAb was added, the uptake in tumor was reduced to 2.2 ± 0.1. With the irrelevant, anti-CD33 mAb the uptake was 0.4 ± 0.1.

Spleen had the second highest uptake for the specific mAb with an activity concentration 1.4 ± 0.2 greater than that of blood. The irrelevant mAb gave a slightly lower value of 0.7 ± 0.1. The increased specific uptake may be due to the accumulation of mAb in sites of occult disease within the spleen. Organ-to-blood activity concentration ratios for free [86]Y approached infinity due to the exceedingly low radioactivity concentration in blood.
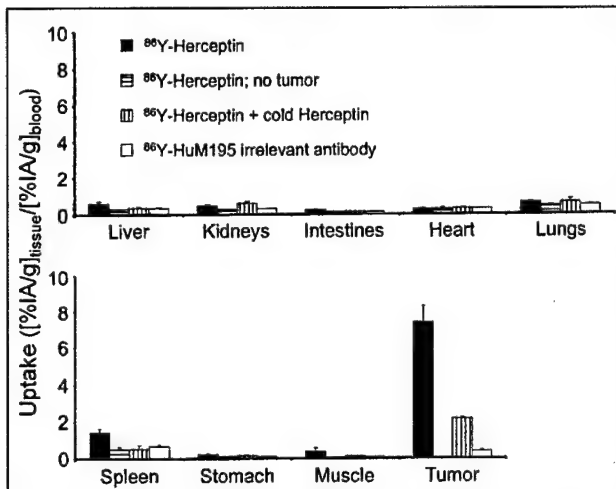

FIGURE 5. Uptake in various tissues 6 d after intraperitoneal injection with [86]Y-trastuzumab ([86]Y-Herceptin), excess unlabeled (cold) trastuzumab, and [86]Y-HuM195. Mean values and SE are shown.

Dosimetry

Absorbed dose to tumor and select organs was calculated for mice receiving ^{90}Y-trastuzumab. Activity concentrations determined from γ-counting dissected tissue was used to scale the ROI contents of the microPET images. The absorbed dose to the kidneys was 0.31 Gy/MBq ^{90}Y-trastuzumab. The liver received 0.48 Gy/MBq, and the spleen received 0.56 Gy/MBq. Because tumors varied in size, calculations were made for spheres of various radii. [90]Y activity was assumed to be uniformly distributed throughout the spheres. Absorbed dose to tumors varied from 0.10 Gy/MBq for radius = 0.1 mm to 3.7 Gy/MBq for radius = 5 mm. Results are summarized in Table 1.

DISCUSSION

There is now a preponderance of evidence to suggest that radioimmunotherapy will be most successful in the treatment

TABLE 1
Absorbed Doses to Organs and Tumors of Varying Sizes After Intraperitoneal Injection of ^{90}Y-Trastuzumab

Organ or tumor	Radius (mm)	Absorbed fraction	Dose (Gy/MBq)
Tumor	0.1	0.017	0.10
Tumor	0.5	0.084	0.48
Tumor	1.0	0.17	0.96
Tumor	3.0	0.45	2.6
Tumor	5.0	0.63	3.7
Liver		0.69	0.48
Kidneys		0.52	0.31
Spleen		0.34	0.56

Calculation based on pharmacokinetics and biodistribution of intraperitoneally injected [86]Y-trastuzumab.

of micrometastatic disease (22–24). Most animal models evaluating tumor response rely on tumor volume measurements obtained by external, caliper-based measurements. Because this approach is not amenable to the evaluation of therapy against micrometastases, the preclinical evaluation of such is usually performed by assessing animal morbidity, secondary to macroscopic growth of the micrometastases (12). Using a positron-emitter–labeled mAb and microPET imaging we have demonstrated the ability to image, monitor targeting kinetics, and perform dosimetry of micrometastases at clinically relevant dimensions, noninvasively.

This approach is fundamentally different from studies examining gene expression, in which a reporter gene is cotransfected with the gene sequence to be studied (25–27). The ability to visualize disease with this approach is critically dependent on the mAb chosen, accessibility of the tumor cells to the injected mAb, and the degree to which the targeted antigen is expressed on tumor cells. These conditions are analogous to the conditions required for successful imaging in patients.

Relative to other small-animal imaging modalities (e.g., optical and MRI), microPET is characterized by a very high sensitivity but limited resolution. The high sensitivity is of great advantage in the detection of minimal disease over the whole body. Using microPET to identify the sites of metastatic spread and then using MRI to image these sites at high resolution, it is possible to use these 2 modalities in a complementary fashion.

The β-particle emitter, ^{90}Y, is one of the most frequently used radionuclides for targeted radionuclide therapy (2,28–30). Recently, the Food and Drug Administration approved use of the ^{90}Y-anti-CD20 mAb (^{90}Y-ibritumomab tiuxetan [Zevalin]; IDEC Pharmaceutical Corp.) for treating various non-Hodgkin's lymphomas (31). ^{90}Y does not emit photons that can be used to obtain pharmacokinetics; biodistribution for dosimetry calculations is, therefore, typically obtained by imaging using the surrogate radiometal ^{111}In. Although this radionuclide has been shown to have a generally similar behavior to ^{90}Y, several differences have been noted (3,4,32). Using the chemically identical positron emitter, ^{86}Y, the true distribution of the therapeutic radionuclide, ^{90}Y, is used in this work.

The methodology outlined in this work for microPET-based dosimetry overcomes several important limitations in direct microPET quantitation. As noted in the methods, microPET quantitation can be influenced by the position of tissue relative to the central axis of the camera and also by the tissue surrounding the ROI. In imaging micrometastases, wherein the activity containing volume is below the intrinsic resolution of the camera, partial-volume effects also become important. These concerns were addressed by relating the time course of PET measurements to γ-counting results and by maintaining ROIs that were greater than the apparent intensity volume.

CONCLUSION

For all injected compounds, the relative microPET image intensity of the tumor matched the subsequently determined ^{86}Y uptake. Coregistration with MR images confirmed the position of ^{86}Y uptake relative to various organs. Radiolabeled trastuzumab mAb was shown to localize to sites of disease with minimal normal organ uptake. Dosimetry calculations showed a strong dependence on tumor size. These results demonstrate the usefulness of combined microPET and MRI for the evaluation of novel therapeutics.

REFERENCES

1. Gordon LI, Witzig TE, Wiseman GA, et al. Yttrium-90 ibritumomab tiuxetan radioimmunotherapy for relapsed or refractory low-grade non-Hodgkin's lymphoma. Semin Oncol. 2002;29(suppl):87–92.
2. Wiseman GA, White CA, Sparks RB, et al. Biodistribution and dosimetry results from a phase III prospectively randomized controlled trial of Zevalin radioimmunotherapy for low-grade, follicular, or transformed B-cell non-Hodgkin's lymphoma. Crit Rev Oncol Hematol. 2001;39:181–194.
3. Lövqvist A, Humm JL, Sheikh A, et al. PET imaging of ^{86}Y-labeled anti-Lewis Y monoclonal antibodies in a nude mouse model: comparison between ^{86}Y and ^{111}In radiolabels. J Nucl Med. 2001;42:1281–1287.
4. Garmestani K, Milenic DE, Plascjak PS, Brechbiel MW. A new and convenient method for purification of ^{86}Y using a Sr(II) selective resin and comparison of biodistribution of ^{86}Y and ^{111}In labeled Herceptin. Nucl Med Biol. 2002;29:599–606.
5. Leyland-Jones B. Trastuzumab: hopes and realities. Lancet Oncol. 2002;3:137–144.
6. Zinner RG, Kim J, Herbst RS. Non-small cell lung cancer clinical trials with trastuzumab: their foundation and preliminary results. Lung Cancer. 2002;37:17–27.
7. Baselga J, Norton L, Albanell J, Kim YM, Mendelsohn J. Recombinant humanized anti-HER2 antibody (Herceptin) enhances the antitumor activity of paclitaxel and doxorubicin against HER2/neu overexpressing human breast cancer xenografts. Cancer Res. 1998;58:2825–2831.
8. Bunn PA Jr, Helfrich B, Soriano AF, et al. Expression of Her-2/neu in human lung cancer cell lines by immunohistochemistry and fluorescence in situ hybridization and its relationship to in vitro cytotoxicity by trastuzumab and chemotherapeutic agents. Clin Cancer Res. 2001;7:3239–3250.
9. Kotts CE, Su FM, Leddy C, et al. ^{186}Re-Labeled antibodies to p185HER2 as HER2-targeted radioimmunopharmaceutical agents: comparison of physical and biological characteristics with ^{125}I and ^{131}I-labeled counterparts. Cancer Biother Radiopharm. 1996;11:133–144.
10. Mujoo K, Maneval DC, Anderson SC, Gutterman JU. Adenoviral-mediated p53 tumor suppressor gene therapy of human ovarian carcinoma. Oncogene. 1996;12:1617–1623.
11. Borchardt P, Quadri SM, Freedman RS, Vriesendorp HM. Intraperitoneal radioimmunotherapy with human monoclonal IGM in nude mice with peritoneal carcinomatosis. Cancer Biother Radiopharm. 2000;15:53–64.
12. McDevitt MR, Ma D, Lai LT, et al. Tumor therapy with targeted atomic nanogenerators. Science. 2001;294:1537–1540.
13. Finn RD, McDevitt M, Ma D, et al. Low energy cyclotron production and separation of yttrium-86 for evaluation of monoclonal antibody pharmacokinetics and dosimetry. In: Duggan JL, Morgan IL, eds. Applications of Accelerators in Research and Industry: Proceedings of the Fifteenth International Conference. Woodbury, NY: American Institute of Physics Press; 1999:991–993.

14. Nikula TK, Curcio MJ, Brechbiel MW, Gansow OA, Finn RD, Scheinberg DA. A rapid, single vessel method for preparation of clinical grade ligand conjugated monoclonal antibodies. *Nucl Med Biol.* 1995;22:387–390.

15. Nikula TK, McDevitt MR, Finn RD, et al. Alpha-emitting bismuth cyclohexyl-benzyl DTPA constructs of recombinant humanized anti-CD33 antibodies: pharmacokinetics, bioactivity, toxicity and chemistry. *J Nucl Med.* 1999;40:166–176.

16. Xu S, Gade TPF, Matei C, et al. In vivo multiple-mouse imaging at 1.5T. *Magn Reson Med.* 2003;49:551–557.

17. Kolbert KS, Hamacher KA, Jurcic JG, Scheinberg DA, Larson SM, Sgouros G. Parametric images of antibody pharmacokinetics in Bi213-HuM195 therapy of leukemia. *J Nucl Med.* 2001;42:27–32.

18. Kolbert KS, Sgouros G, Scott AM, et al. Implementation and evaluation of patient-specific three-dimensional internal dosimetry. *J Nucl Med.* 1997;38:301–308.

19. Loevinger R, Budinger T, Watson E. *MIRD Primer For Absorbed Dose Calculations.* New York, NY: Society of Nuclear Medicine; 1988:1–17.

20. Bardies M, Chatal JF. Absorbed doses for internal radiotherapy from 22 beta-emitting radionuclides: beta dosimetry of small spheres. *Phys Med Biol.* 1994;39:961–981.

21. Kolbert KS, Watson T, Matei C, Xu S, Koutcher JA, Sgouros G. Murine S factors for liver, spleen, and kidney. *J Nucl Med.* 2003;44:784–791.

22. Goldenberg DM. Targeted therapy of cancer with radiolabeled antibodies. *J Nucl Med.* 2002;43:693–713.

23. DeNardo SJ, Williams LE, Leigh BR, Wahl RL. Choosing an optimal radioimmunotherapy dose for clinical response. *Cancer.* 2002;94(suppl):1275–1286.

24. Mattes MJ. Radionuclide-antibody conjugates for single-cell cytotoxicity. *Cancer.* 2002;94(suppl):1215–1223.

25. Jacobs A, Tjuvajev JG, Dubrovin M, et al. Positron emission tomography-based imaging of transgene expression mediated by replication-conditional, oncolytic herpes simplex virus type 1 mutant vectors in vivo. *Cancer Res.* 2001;61:2983–2995.

26. Doubrovin M, Ponomarev V, Beresten T, et al. Imaging transcriptional regulation of p53-dependent genes with positron emission tomography in vivo. *Proc Natl Acad Sci USA.* 2001;98:9300–9305.

27. Gambhir SS, Herschman HR, Cherry SR, et al. Imaging transgene expression with radionuclide imaging technologies. *Neoplasia.* 2000;2:118–138.

28. Waldherr C, Pless M, Maecke HR, Haldemann A, Mueller-Brand J. The clinical value of [90Y-DOTA]-D-Phe1-Tyr3-octreotide (90Y-DOTATOC) in the treatment of neuroendocrine tumours: a clinical phase II study. *Ann Oncol.* 2001;12:941–945.

29. Paganelli G, Zoboli S, Cremonesi M, et al. Receptor-mediated radiotherapy with 90Y-DOTA-D-Phe1-Tyr3-octreotide. *Eur J Nucl Med.* 2001;28:426–434.

30. Richman CM, DeNardo SJ. Systemic radiotherapy in metastatic breast cancer using 90Y-linked monoclonal MUC-1 antibodies. *Crit Rev Oncol Hematol.* 2001;38:25–35.

31. Crawford LM Jr. From the Food and Drug Administration. *JAMA.* 2002;287:1640.

32. Clarke K, Lee F-T, Brechbiel MW, Smyth FE, Old LJ, Scott AM. In vivo biodistribution of a humanized anti-Lewis Y monoclonal antibody (hu3S193) in MCF-7 xenografted BALB/c nude mice. *Cancer Res.* 2000;60:4804–4811.

Alpha-Particle Emitting Atomic Generator (Actinium-225)-Labeled Trastuzumab (Herceptin) Targeting of Breast Cancer Spheroids: Efficacy *versus* HER2/*neu* Expression

Åse M. Ballangrud, Wei-Hong Yang, Stig Palm, Richard Enmon, Paul E. Borchardt, Virginia A. Pellegrini, Michael R. McDevitt, David A. Scheinberg, and George Sgouros

Memorial Sloan-Kettering Cancer Center, New York, New York

ABSTRACT

Purpose: The humanized monoclonal antibody, trastuzumab (Herceptin), directed against HER2/*neu*, has been effective in the treatment of breast cancer malignancies. However, clinical activity has depended on HER2/*neu* expression. Radiolabeled trastuzumab has been considered previously as a potential agent for radioimmunotherapy. The objective of this study was to investigate the efficacy of trastuzumab labeled with the α-particle emitting atomic generator, actinium-225 (^{225}Ac), against breast cancer spheroids with different HER2/*neu* expression levels. ^{225}Ac has a 10-day half-life and a decay scheme yielding four α-particles.

Experimental Design: The breast carcinoma cell lines MCF7, MDA-MB-361 (MDA), and BT-474 (BT) with relative HER2/*neu* expression (by flow cytometry) of 1:4:18 were used. Spheroids of these cell lines were incubated with different concentrations of ^{225}Ac-trastuzumab, and spheroid growth was measured by light microscopy over a 50-day period.

Results: The activity concentration required to yield a 50% reduction in spheroid volume at day 35 was 18.1, 1.9, and 0.6 kBq/ml (490, 52, 14 nCi/ml) for MCF7, MDA, and BT spheroids, respectively. MCF7 spheroids continued growing but with a 20–30 day growth delay at 18.5 kBq/ml. MDA spheroid growth was delayed by 30–40 days at 3.7 kBq/ml; at 18.5 kBq/ml, 12 of 12 spheroids disaggregated after 70, days and cells remaining from each spheroid failed to form colonies within 2 weeks of being transferred to adherent dishes. Eight of 10 BT spheroids failed to regrow at 1.85 kBq/ml. All of the BT spheroids at activity concentrations 3.7 kBq/ml failed to regrow and to form colonies. The radiosensitivity of these three lines as spheroids was evaluated as the activity concentration required to reduce the treated to untreated spheroid volume ratio to 0.37, denoted DVR_{37}. An external beam radiosensitivity of 2 Gy was found for spheroids of all three of the cell lines. After α-particle irradiation a DVR_{37} of 1.5, 3.0, and 2.0 kBq/ml was determined for MCF7, MDA, and BT, respectively.

Conclusion: These studies suggest that ^{225}Ac-labeled trastuzumab may be a potent therapeutic agent against metastatic breast cancer cells exhibiting intermediate to high HER2/*neu* expression.

INTRODUCTION

The humanized monoclonal antibody, trastuzumab, directed against HER2/*neu*, particularly in combination with chemotherapy, has been effective in the treatment of breast cancer malignancies overexpressing HER2/*neu* (1–4). This work examines a treatment approach using trastuzumab labeled with the α-particle emitting atomic generator, actinium-225 (^{225}Ac), to eradicate breast cancer metastases expressing variable levels of HER2/*neu*.

The HER2/*neu* oncogene encodes a transmembrane protein (p185^{HER2}) with extensive homology to the epidermal growth factor receptor. Amplification and overexpression of HER2/*neu* have been documented in many human tumors, most notably in breast cancer (5, 6). The expression of HER2/*neu* is relatively stable over time and is generally congruent at different metastatic sites (5, 7). However, HER2/*neu* protein has also been identified on cell membranes of epithelial cells in the gastrointestinal, respiratory, reproductive, and urinary tract, as well as in the skin, breast, and placenta. HER2/*neu* expression levels in these normal tissues are similar to the levels found in nonamplified, nonoverexpressing breast cancers cells (6). Approximately 30% of breast cancer patients have tumors overexpressing the HER2/*neu* receptor. Trastuzumab treatment has been limited to these patients because of the cross-reactivity with normal tissues noted above. HER2/*neu* has been considered previously as a target for radioimmunotherapy against breast cancer. The radionuclides, ^{131}I, ^{125}I, ^{186}Re (8, 9), the positron-emitter, ^{86}Y (10), and also ^{212}Pb (11), of which the daughter, ^{212}Bi, decays by α-particle emission, have been labeled to antibodies targeting HER2/*neu* and investigated in animal models.

The α-particle emitting atomic generator, ^{225}Ac, has a 10-day half-life, and each decay of ^{225}Ac leads to the emission of four α particles (Fig. 1), greatly increasing its efficacy over previously considered α-particle emitters (12–14). Studies, *in vitro* and in animal models, have shown that this radionuclide is ~1000-fold more effective per unit radioactivity than ^{213}Bi, a first generation α-emitter that is currently under clinical inves-

^{225}Ac (10 d)

5.8 MeV

^{221}Fr (4.9 m)

6.4 MeV

^{217}At (32 ms)

7.1 MeV

^{213}Bi (45.6 m)

98% ^{213}Po (4.3 μs)

5.8 MeV 2%

8.4 MeV

^{209}Tl (2.2 m)
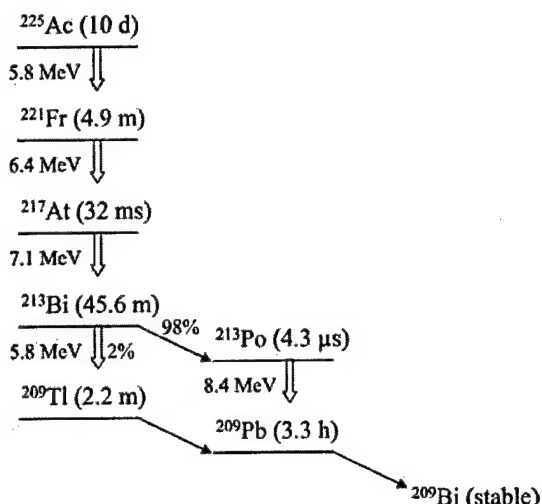
^{209}Pb (3.3 h)

^{209}Bi (stable)

Fig. 1 Simplified decay scheme for actinium-225 (*^{225}Ac*). The *arrows* designate decay by α-particle emission; the average energy of emitted α-particles is shown next to each arrow.

tigation (15, 16). Studies in animals, however, have also shown that depending on the administration route, target, and chelation chemistry, it is also substantially more toxic (17–19). The increased efficacy arises because ^{225}Ac has a longer half-life (10 days *versus* 45.6 min for ^{213}Bi), increasing the total number of decays per unit of radioactivity, allowing prolonged irradiation of targeted cells, and because its decay leads to the release of three α-particle emitting daughters. The toxicity arises because chelate conjugated antibody delivery of this radionuclide can only retain, within the chelate, the first of the four α-emitting atoms. The chelation of the radionuclide is disrupted upon transformation of the parent atom, and emission of the first α. Subsequent α-emitting daughter atoms are, therefore, free to possibly distribute elsewhere in the body and potentially irradiate normal organs. This will be mitigated if the radiolabeled antibody is internalized, because charged daughter atoms produced intracellularly are retained within the cell (18).

Such a treatment strategy has been investigated, *in vitro*, using the spheroid model to represent rapidly accessible, intravascularly distributed tumor cell clusters (20). In anticipation of variable HER2/*neu* expression in a particular population of breast carcinoma cells, efficacy against cells with different HER2/*neu* expression levels has been examined. In contrast to traditional radioimmunotherapy with β-particle emitters, which kill cells over a large, multi-mm range, α-particles can kill individual cells; therefore, antigen density on the target cell will play an accordingly greater role in efficacy.

MATERIALS AND METHODS

Cells. The breast carcinoma cell lines MCF7, MDA-MB-361 (MDA), and BT-474 (BT) were purchased from the American Type Culture Collection (Manassas, VA). MCF7 monolayer cultures were incubated in MEM with NEAA (Memorial Sloan-Kettering Cancer Center Media Lab, New York, NY), MDA in L-15 (Memorial Sloan-Kettering Cancer Center Media

Lab), and BT in RPMI with 10 mM HEPES, 1 mM NA pyruvate, 2 mM L-glutamine, 1.5g/liter bicarbonate, and 4.5g/liter glucose (MSKCC Media Lab). The medium for all of the cell lines was supplemented with 10% fetal bovine serum, 100 units/ml penicillin, and 100 μg/ml streptomycin. The cell cultures were kept at 37°C in a humidified 5% CO_2 and 95% air incubator.

Spheroids. Spheroids were initiated using the liquid overlay technique of Yuhas *et al.* (21) and Ballangrud *et al.* (22). Approximately 10^6 cells, obtained by trypsinization from growing monolayer cultures, were seeded into 100-mm dishes coated with a thin layer of 1% agar (Bacto Agar; Difco, Detroit, MI) with 15 ml of medium. The medium used was the same as for monolayer cultures. After 5–7 days, spheroids with approximate diameters of 200 ± 20 μm were selected under an inverted phase-contrast microscope with an ocular scale using an Eppendorf pipette. The selected spheroids were transferred to 35-mm bacteriological Petri dishes in 2-ml medium for treatment.

Spheroids selected for disaggregation were centrifuged at 100 × g for 1 min to remove medium. The pellet was then suspended and gently mixed in preheated (37°C) PBS contain-
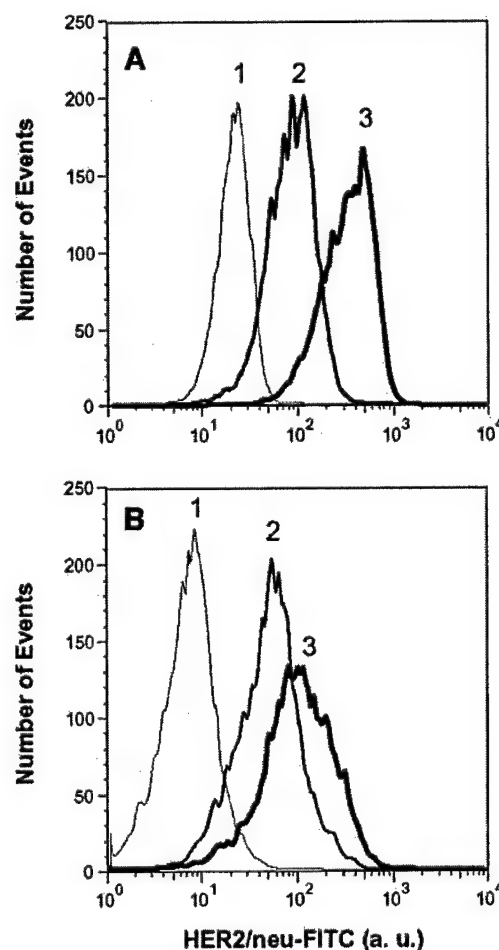
Fig. 2 Expression of HER2/*neu* as determined by flow cytometry of (*A*) cells from monolayer culture and (*B*) cells from disaggregated spheroids. Traces 1, 2, and 3 correspond to MCF7, MDA-MB-361, and BT-474 cells, respectively.
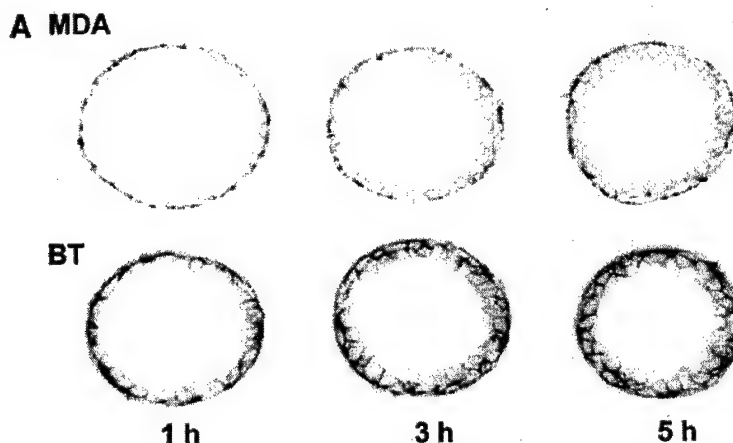
A MDA

BT

1 h   **3 h**   **5 h**

Fig. 3 A, confocal microscopy images of spheroids (φ~ 200 mm) after 1-, 3-, and 5-h incubation with 10 μg/ml trastuzumab-FITC. The *black* or *gray* regions reflect presence of trastuzumab. Individual cells are clearly outlined in the surface layer of MDA-MB-361 (*MDA*) and BT-474 (*BT*) spheroids, consistent with cell-surface localization of HER2/*neu*. At 10 μg/ml trastuzumab-FITC, no uptake of trastuzumab was observed in MCF7 spheroids. Also shown, trastuzumab concentration profiles across the spheroid equator after 1-, 3-, and 5-h incubation with 10 μg/ml trastuzumab-FITC for (*B*) MDA and (*C*) BT spheroids. The mean of five individual spheroid measurements are depicted; *bars,* ±SE.
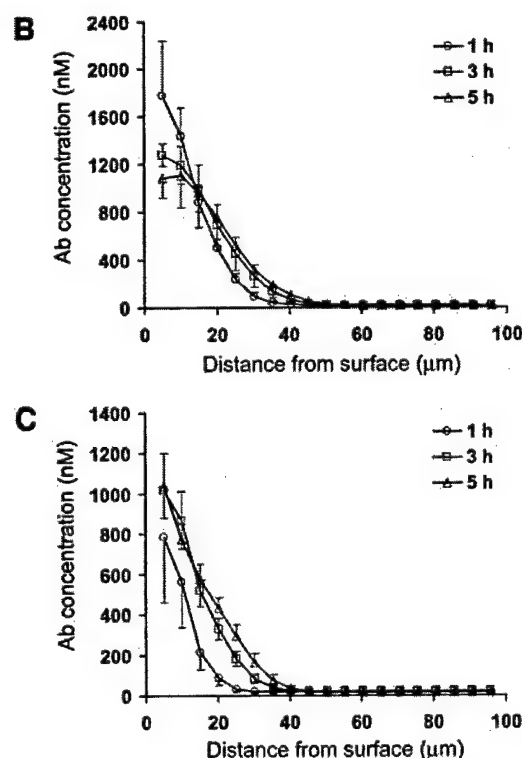
ing 0.25% trypsin and 1 mM EDTA. Light microscopy was used to monitor the mixture for spheroid dissociation and membrane blebbing as an early indicator of membrane rupture. Dissociation normally occurred within 2 min, during which blebbing of cells was minimal. The suspension was immediately centrifuged at 75 × g for 45 s to remove trypsin and the pellet resuspended in PBS for flow cytometry.

Flow Cytometry. The relative level of HER2/*neu* expression for the three cell lines was determined using the Becton-Dickinson FACSCalibur Analyzer (Franklin Lakes, NJ). HER2/*neu* expression was determined for cells from both monolayer culture and from disaggregated spheroids. All of the

washes and incubations were performed in FACS buffer (PBS +0.5% BSA +0.02% NaN$_3$). Cells were washed twice and resuspended at 1–2 × 10^6 cells/ml. A 100-μl aliquot was incubated with trastuzumab for 0.5 h on ice. Cells were again washed twice and resuspended in 100 μl buffer. The secondary, fluorescently tagged antibody, against the F$_c$ portion of human IgG (Sigma; F-9512), was added and the suspension incubated on ice for 0.5 h. After a final two washes, cells were resuspended in 2 ml of cold buffer and analyzed. A total of 10,000 events were collected for each cell line.

Antibodies. Trastuzumab (anti-HER2/*nue*; Genentech, Inc., South San Francisco, CA) was used as the specific anti-
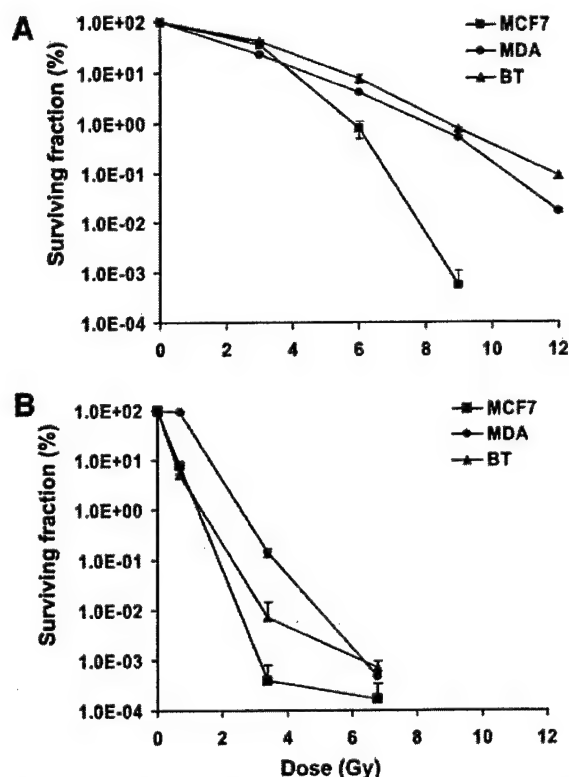
Fig. 4 Surviving fraction of MCF7, MDA-MB-361 (*MDA*), and BT-474 (*BT*) cells in monolayer cultures are shown after (*A*) acute doses of external beam radiation and (*B*) 24-h incubation with 3.7, 18.5, and 37 kBq/ml actinium-225-labeled nonspecific antibody, corresponding to absorbed doses of 0.7, 3.4, and 6.8 Gy, respectively; *bars*, ±SE.

body. HuM195 (anti-CD33; Protein Design Laboratories, Inc., Sunnyview, CA) and J591 (anti-PSMA; generously supplied by Dr. Neil Bander, Department of Urology, New York Presbyterian Hospital-Weill Medical College of Cornell University and Ludwig Institute for Cancer Research, New York, NY) were used as nonspecific controls.

Confocal Microscopy. Spheroids of diameter 200 μm were incubated with 10 μg/ml FITC- (F7250; Sigma, St. Louis, MO) conjugated trastuzumab for 1, 3, and 5 h and imaged by confocal microscope (Zeiss LSM 510; Carl Zeiss, Inc. Oberkochen, Germany) while still in incubation medium. A 3-μm-thick optical section was acquired at the center of each spheroid. Five spheroids were imaged for each time point. Antibody concentration as a function of radial distance was obtained using MIAU, a software package developed in-house (23). The method has been described previously (24). Briefly, an erosion element is used to follow the exterior contour of each spheroid, and the average pixel intensity in each ring is converted to antibody concentration by calibration with the known external concentration of antibody. The antibody concentration as a function of distance from the rim of the spheroid was corrected for light attenuation as described previously (24).

[225]Ac. [225]Ac was obtained from the Department of Energy (Oak Ridge National Laboratory, Oak Ridge, TN) and was supplied as a dried nitrate residue. The [225]Ac activity was measured with a Squibb CRC-17 Radioisotope Calibrator (E.R. Squibb and Sons, Inc., Princeton, NJ) set at 775 and multiplying the displayed activity value by 5. The [225]Ac nitrate residue was dissolved in 0.1 ml of 0.2 M Optima grade HCl (Fisher Scientific, Pittsburgh, PA). Metal-free water used for this and all of the other solutions was obtained from a Purelab Plus system (United States Filter Corp., Lowell, MA) and was sterile filtered.

Radiolabeling. Details regarding the radiolabeling methodology are described in reference (13).

The first step in construct preparation was the [225]Ac-1,4,7,10-tetraazacyclododecane-*N,N',N'',N'''* -tetraacetic acid (DOTA)-neocarzinostatin chelation reaction. The bifunctional isothiocyanato-derived 2B-DOTA, 2-(*p*-isothiocyanatobenzyl)-1,4,7,10-tetraazacyclododecane-1,4,7,10-tetraacetic acid was obtained from Macrocyclics (Dallas, TX). [225]Ac dissolved in 0.2 M HCl was mixed with 200–500 mg of 10 g/liter DOTA-neocarzinostatin in metal-free water, 0.015–0.020 ml of 150 g/liter stock *l*-ascorbic acid, and 0.025–0.150 ml of 2 M tetramethylammonium acetate. The mixture was then heated to 60°C for 30–45 min.

The second step in construct preparation was the [225]Ac-DOTA- neocarzinostatin reaction with the IgG. The [225]Ac-DOTA- neocarzinostatin chelation reaction was mixed with 0.5–1.0 mg of the IgG, 0.015–0.020 ml of 150 g/liter stock *l*-ascorbic acid, and 0.025–0.150 ml of a 1 M carbonate buffer. The reaction mixture was then heated to 36°C for 30–60 min. At the end of the reaction period, the mixture was treated with a 0.020-ml addition of 10 mM diethylenetriaminepentaacetic acid to complex any free metals during the size exclusion chromatographic purification using a 10 DG size exclusion column with a 1% human serum albumin as the mobile phase.

The radiochemical purity of [225]Ac-DOTA-trastuzumab was >90% as determined by instant TLC methods, and the immunoreactivity of the labeled product was between 70% and 80% as determined by cell-based assay methods (25).

Radiosensitivity. The radiosensitivity of the different cell lines was determined in monolayer cultures using the colony-forming assay (26). Depending on the radiation dose, between 10^3 and 10^7 cells were plated in monolayer cultures. External beam radiosensitivity was determined after exposure to acute doses of 3, 6, 9, or 12 Gy photon irradiation using a cesium irradiator at a dose rate of 0.8 Gy/min (Cs-137 Model 68; JL Shepherd and Associates, Glendale, CA.). The absorbed dose required to yield a 37% survival in the log-linear portion of the surviving fraction curve (*i.e.,* the D_0 value) was obtained by fitting a monoexponential function to this portion of the curve.

Table 1 Dose, D_0, required to reduce surviving fraction of cells in monolayer cultures following external beam and α-particle irradiation to 0.37

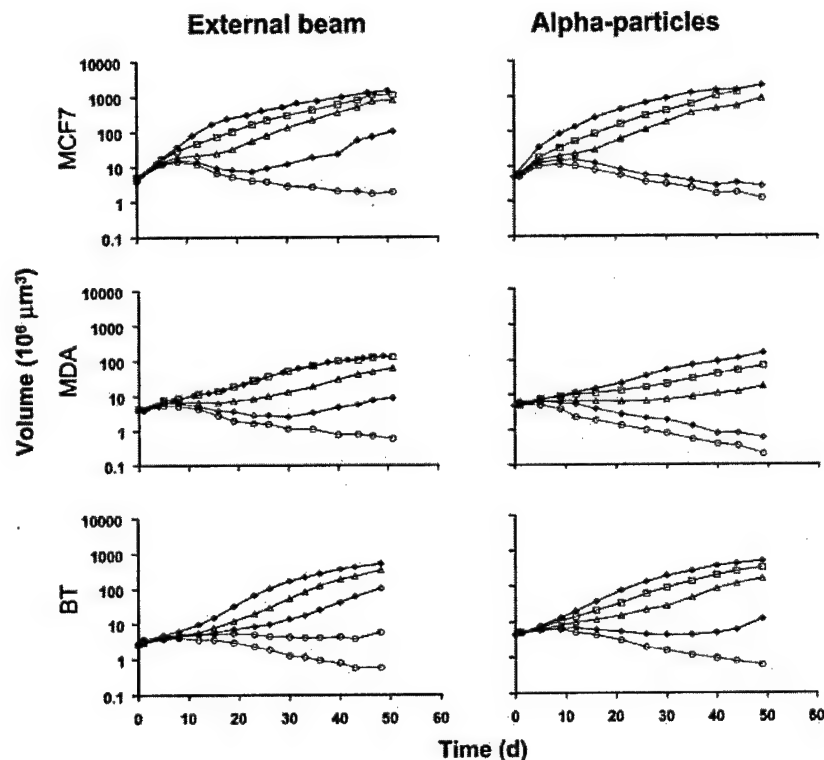| Cell line	External beam D_0 (Gy)	α-Particle D_0 (Gy)
MCF7	0.76 ± 0.07	0.27 ± 0.02
MDA[a]	1.38 ± 0.01	0.53 ± 0.03
BT	1.73 + 0.01	0.37 ± 0.05

[a] MDA, MDA-MB-361; BT, BT-474.

External beam   Alpha-particles

Fig. 5 Spheroid response to external beam irradiation (♦, untreated; □, 3 Gy; △, 6 Gy; ◇, 9 Gy; ○, 12 Gy) and increasing concentrations of actinium-225-labeled nonspecific antibody (♦, untreated; □, 1.85 kBq/ml; △, 3.70 kBq/ml; ◇, 9.25 kBq/ml; ○, 18.5 kBq/ml).

Monolayer cultures incubated with 3.7, 18.5, and 37 kBq/ml [225]Ac-labeled nonspecific antibody for 24 h were used to determine α-particle radiosensitivity. Over a 24-h period, 6.7% of the total number of [225]Ac atoms will have decayed. Because the longest-lived daughter, Bi-213, has a half-life of 45.6 min, all of the daughters generated during this period will also decay. Assuming, therefore, that each decay of [225]Ac deposits one-half (to account for cells settling to the bottom of the plate and, therefore, being irradiated only from one side) of the sum of all four of the α-particle energies, the mean absorbed dose is estimated to be 0.7, 3.4, and 6.8 Gy for each of the three concentrations, respectively.

The radiosensitivity of spheroids was evaluated as the activity concentration required to reduce the treated to untreated spheroid volume ratio to 0.37. Because this parameter depends on the day post-therapy, volume ratios from day 20 to day 45 after therapy were calculated for each spheroid, and the median value across this time period was used. By plotting this volume ratio *versus* activity concentration and fitting the log-linear portion of the curve to a monoexponential function, a radiosensitivity parameter may be derived from the slope. The inverse of the slope gives the dose that yields a volume ratio of 0.37. This value is denoted "DVR_{37}," and it is loosely analogous to the D_0 in colony formation assays.

Treatment Protocol. The response to [225]Ac-labeled trastuzumab was evaluated by incubating spheroids with 0.37, 1.85, 3.70, or 18.50 kBq/ml [225]Ac on 10 μg/ml trastuzumab (specific antibody) for 1 h. Spheroids exposed to 18.50 kBq/ml [225]Ac on 10 μg/ml irrelevant antibody (radioactive control), 10 μg/ml unlabeled trastuzumab (unlabeled antibody control), and un-

treated spheroids (control) were followed in the same manner. Twenty-four or 12 spheroids were used in each experiment. After incubation, the spheroids were washed three times by suspension in fresh medium and placed in separate wells of a 24-well plate. The medium in each well was replaced, and individual spheroid volume measurements were performed twice per week. An inverted phase microscope fitted with an ocular micrometer was used to determine the major and minor diameter d_{max} and d_{min}, respectively, of each spheroid. Spheroid volume was calculated as $V = \pi \cdot d_{max} \cdot d_{min}^2 / 6$. Volume monitoring was stopped once a spheroid diameter exceeded 1 mm or when the spheroid fragmented to individual cells or smaller (2–3-cell) clusters. The viability of such fragments was assessed in an outgrowth assay by plating the cell clusters on to adherent dishes, incubating for 2 weeks, and then evaluating for colony formation or outgrowth.

RESULTS

The relative HER2/*neu* cell-surface expression of MCF7, MDA, and BT cells derived from monolayer culture and from disaggregated spheroids is depicted in Fig. 2. The highest HER2/*neu* expressing cell line, BT, shows a decrease in the number of HER2/*neu* sites (relative to MDA) and also a greater variability in cell surface expression in cells derived from spheroids compared with cells from monolayer culture. The relative expression of HER2/*neu* in cells derived from monolayers is 1:4:18 (MCF7:MDA:BT); the corresponding expression ratios for cells derived from spheroids are 1:6:12.

Penetration of trastuzumab into spheroids was evaluated by

measuring FITC-labeled trastuzumab by confocal microscopy. Images acquired through the equator of 200-μm diameter spheroids incubated for 1, 3, and 5 h with 10 μg/ml trastuzumab-FITC are shown for MDA and BT spheroids in Fig. 3*A*. The cells on the spheroid rim are clearly outlined, consistent with antibody localization to cell-surface HER2/*neu*. Trastuzumab has penetrated ~1, 2, and 3 cell layers after 1-, 3-, and 5-h incubation, respectively. FITC intensity was converted to antibody concentration as described in "Materials and Methods." The results are depicted in Fig. 3, *B* and *C*. After 1-h incubation, the concentration of antibody on the surface of BT spheroids is greater than twice that on the surface of MDA spheroids. At a depth of 20 μm, the antibody concentration in BT spheroids is 5-fold greater than in MDA spheroids.

To examine for a possible differential sensitivity to unlabeled trastuzumab antibody, spheroids of the three cell lines were incubated for 1 h in 10, 50, 100, and 500 μg/ml. No impact on spheroid growth was observed (data not shown).

To discriminate between inherent radiosensitivity of the different cell lines and increased targeting due to the differential expression of HER2/*neu*, the radiosensitivity of each cell line was determined in monolayer cultures as well as by following spheroid growth after external beam irradiation and after incubation with ^{225}Ac-labeled nonspecific antibody. The surviving fraction of cells in monolayer culture is plotted *versus* mean absorbed dose for photons and α-particles in Fig. 4, *A* and *B*, respectively. The dose, D_0, required to yield a surviving fraction of 37% is listed in Table 1. MCF7 cells are 2-fold and 2.4-fold more sensitive to external beam radiation than MDA and BT cells, respectively. Although this cell line is also more sensitive to α-particle radiation than MDA and BT, the differences in radiosensitivity are less pronounced.

Spheroid response to 3, 6, 9, and 12 Gy external beam irradiation and increasing concentrations of ^{225}Ac-labeled nonspecific antibody (24 h incubation) is depicted in Fig. 5. Fifty days after a 12 Gy external dose, outgrowth assays for MCF7 and BT spheroids showed viable cells, whereas no colonies were formed for MDA spheroids. At the two highest concentrations of ^{225}Ac-labeled nonspecific radiolabeled antibody, outgrowth assays for MCF7 and MDA spheroids yielded no colonies; for BT the same result was obtained only at the highest radioactivity concentration used. The dose required to reduce the volume ratio of treated to untreated spheroids to 0.37, denoted DVR_{37}, was used as a measure of spheroid radiosensitivity and is listed in Table 2. The DVR_{37} results show no difference among spheroids of the three cell lines in sensitivity to external beam irradiation. Differences in volume response to α-particle irradiation are seen, however, with MCF7 almost a factor of 2 more sensitive than MDA.

Fig. 6 Median growth curves for spheroids incubated 1 h with 0.37 (*), 1.85 (◇), 3.7 (□), and 18.5 (●) kBq/ml actinium-225 on 10 μg/ml trastuzumab, or 18.5 kBq/ml on nonspecific antibody (radioactive control; ○).

Median growth curves for MCF7, MDA, and BT spheroids incubated 1 h with 0.37, 1.85, 3.7, and 18.5 kBq/ml ^{225}Ac on 10 μg/ml trastuzumab or 18.5 kBq/ml on nonspecific antibody (radioactive control) are depicted in Fig. 6. At day 35, the median volume of spheroids treated with 18.5 kBq/ml ^{225}Ac-trastuzumab relative to spheroids incubated for 1 h with ^{225}Ac-labeled nonspecific antibody (radioactive control) was 52%, 1.4%, and 0.3% for MCF7, MDA and BT, respectively. The ^{225}Ac activity concentration required to yield a 50% reduction in spheroid volume relative to the radioactive controls at day 35 was 18.1, 1.9, and 0.6 kBq/ml (490, 52, 14 nCi/ml) for MCF7, MDA, and BT spheroids, respectively. Growth of individual spheroids after 1 h of incubation with increasing concentrations of ^{225}Ac on 10 μg/ml trastuzumab are shown in Fig. 7. The variability in response of individual spheroids was minimal. At an activity concentration of 1.85 kBq/ml, 2 of 12 BT spheroids were viable; no colonies were observed at 3.7 and 18.5 kBq/ml for this cell line. Likewise, no colonies were observed for MDA spheroids treated at 18.5 kBq/ml. Fig. 8 depicts optical microscope images of MDA spheroids after ^{225}Ac-trastuzumab treatment. By 21 days after incubation with 3.7 kBq/ml sloughing of cells may be observed; by 42 days, however, the spheroid appears to have recovered. At 18.5 kBq/ml, however, no such recovery is observed.

Table 2 Dose required to reduce the treated to untreated spheroid volume ratio to 0.37 (DVR_{37})

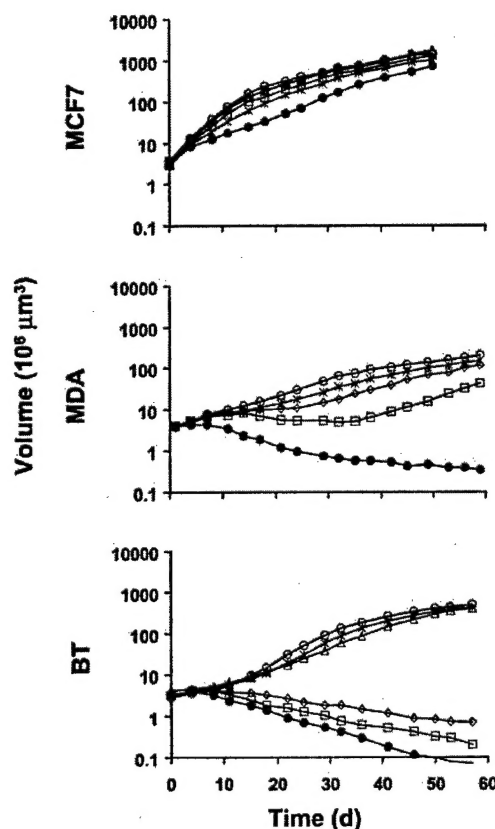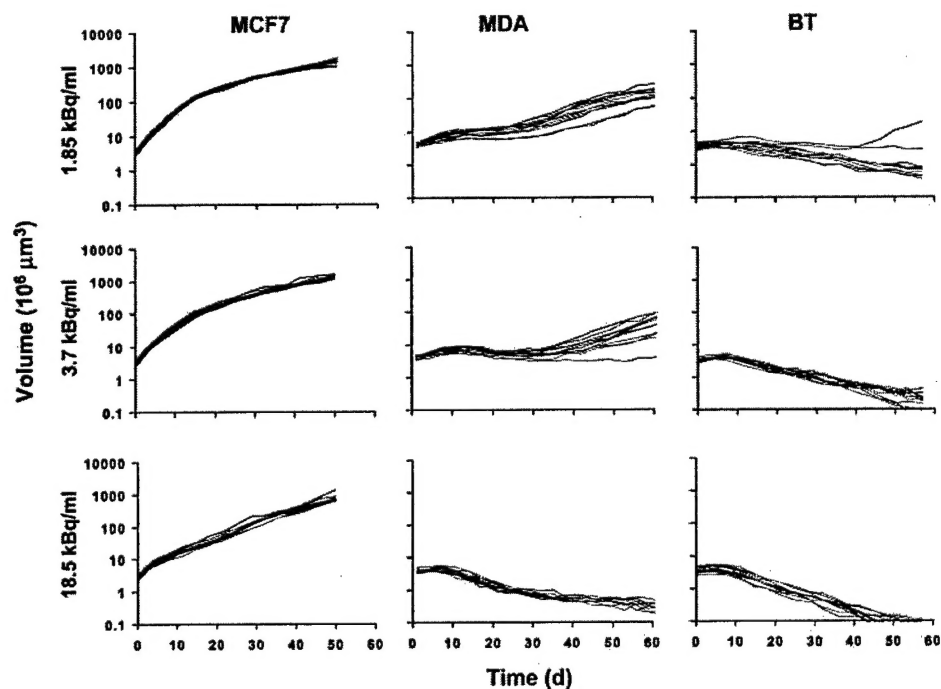| Cell line	External beam DVR_{37} (Gy)	α-Particle DVR_{37} (kBq/ml)
MCF7	2.2 ± 0.2	1.6 ± 0.3
MDA[a]	2.1 ± 0.1	3.0 ± 0.8
BT	2.7 ± 0.4	2.5 ± 0.7

[a] MDA, MDA-MB-361; BT, BT-474.

Fig. 7 Growth of individual spheroids after 1 h incubation with actinium-225-trastuzumab. Each *curve* corresponds to an individual spheroid. Twelve spheroids were used per experiment.

DISCUSSION

Trastuzumab-mediated targeting of ^{225}Ac to disseminated breast cancer will be a viable therapeutic approach in humans only if two fundamental problems are addressed. First, the high background expression of HER2/*neu* in normal tissues must be obviated, as this cross-reactivity is likely to lead to α-particle irradiation of normal tissues. Second, the potential toxicity associated with the distribution of free, α-particle emitting daughters resulting from the decay of ^{225}Ac must be overcome.

Both of these requirements may be met by targeting rapidly accessible micrometastatic disease in a treatment schedule in which i.v. administered ^{225}Ac-trastuzumab is allowed to distribute for several hours and is then cleared from the circulation, either by direct physical means such as plasmapheresis or immunoadsorption (27, 28). Extravasation of intact antibody into normal tissue parenchyma generally requires 24–48 h (29). By rapidly decreasing the concentration of circulating antibody, binding to normal cross-reactive tissues would be reduced sub-

Fig. 8 Microscope images of two treated (3.7 kBq/ml and 18.5 kBq/ml) and one untreated (*control*) MDA-MB-361 spheroid after 1, 21, 42, and 59 days of 1-h incubation with actinium-225 (^{225}Ac)-trastuzumab.

control

3.7 kBq/ml
^{225}Ac-Herceptin

18.5 kBq/ml
^{225}Ac-Herceptin

stantially, whereas also reducing the ^{225}Ac concentration in the circulation and, therefore, the subsequent concentrations of free daughters.

We have used the spheroid model as a preliminary *in vitro* model to examine the feasibility of targeting breast cancer micrometastases using trastuzumab labeled with the atomic α-particle generator, ^{225}Ac. In particular, the efficacy against tumor cell clusters with different expression levels of HER2/*neu* was examined. As demonstrated by flow cytometry, the three cell lines considered approximated low (MCF7), intermediate (MDA MB-361), and high (BT-474) HER2/*neu* expressing metastases. The 1:4:18 relative cell-surface HER2/*neu* expression levels for MCF7:MDA:BT are of comparable magnitude to the 1:14:21 values calculated from data reported by Lewis *et al.* (30). Differences in the actual values may be explained by the different agents and incubation conditions used to perform the measurements. In a previous report (30), cells were incubated with the murine-derived anti-HER2/*neu* antibody 4D5 and also with a fluorescently labeled F(ab')$_2$ fragment of goat antimouse IgG. In the current studies, incubation was carried with the humanized version of 4D5, trastuzumab. The cells were subsequently incubated with a commercially available fluorescently tagged antihuman F$_c$ antibody.

Antibody penetration relative to cell-surface antigen density was also examined. The trastuzumab concentration in BT spheroids after 1-h incubation was found to be a factor 2–3 higher than for the MDA spheroids, whereas the penetration depth into the spheroids was similar. The antibody concentration used is close to the average receptor concentration within the spheroid. Assuming 10^6 receptors per cell (31) and ~4 × 10^{11} cells/liter (24), the concentration of receptor sites within the BT spheroid is ~660 nM. Because 10 μg/ml intact antibody translates to ~670 nM, the concentration of antibody matches, and, due to the large antibody supply, would saturate available cell-surface receptor sites (27, 32). The confocal microscopy studies are consistent with this analysis.

Trastuzumab incubation in monolayer cultures is reported to result in increased cell doubling time leading to increased cell dormancy (30). This was not observed in spheroids where we found that a 1-h incubation with concentrations up to 500 μg/ml trastuzumab had no effect on spheroid growth kinetics for the three cell lines tested. The absence of an effect on spheroids as opposed to monolayer cultures is probably the result of the very short incubation duration, the resulting incomplete penetration of the antibody and also possibly due to the increased resistance of spheroids *versus* monolayer cultures to growth inhibitory agents (33).

The differences in response of the three cell lines cannot be attributed to differences in radiosensitivity, because MCF7 spheroids, having the lowest response to ^{225}Ac-trastuzumab, were also the most radiosensitive. In monolayer cultures, MDA and BT were approximately equivalent in photon radiosensitivity, whereas MCF7 was ~2-fold more radiosensitive. MCF7 was also the line most sensitive to α-particle radiation, and MDA was the lowest in sensitivity to α. MCF7, MDA, and BT spheroids were found to have similar external beam radiosensitivity. Spheroids were found to have a greater differential sensitivity to α-particles than to external beam irradiation, although the opposite is true in monolayer cultures. It is important to note

that the radiosensitivity parameter defined in this work for spheroids is not a measure of cell sterilization but rather of volume reduction. Volume reduction encompasses a number of biological variables including the rates of cellular sterilization, removal of sterilized cells, and cellular proliferation.

As in other studies investigating the relationship between HER2/*neu* expression and growth inhibition using chemotherapeutic and biological agents (30, 34), the response of spheroids to ^{225}Ac-trastuzumab was found to be highly dependent on HER2/*neu* expression. It was possible to sterilize spheroids with intermediate HER2/*neu* expression and to induce a growth delay in low HER2/*neu*-expressing spheroids by increasing the specific activity of the radiolabeled antibody. A very high specificity relative to the radioactive controls was observed. This is because targeted spheroids are exposed to the atomic α-particle generator for a prolonged time period due to binding and retention of the antibody. Longer radioactive control exposure durations such as the 24-h period used in the radiosensitivity measurements showed volume reductions similar to those obtained with the 1 h specific antibody incubation. The very high specificity seen with a short exposure time supports the clearing strategy outlined above.

In conclusion, we have demonstrated the ability to increase the efficacy of trastuzumab against clusters of tumors cells expressing intermediate levels of HER2/*neu* by labeling trastuzumab with the α-particle emitting atomic generator, ^{225}Ac. These results suggest that an ^{225}Ac concentration in the range 0.6–2 kBq/ml (20–75 nCi/ml) may be sufficient to achieve a substantial reduction in the number of tumor cells with intermediate HER2/*neu* expression. This translates to approximately 0.07–0.3 mCi for human administration. On the basis of animal studies, we expect that this activity concentration will be clinically implementable.

REFERENCES

1. Baselga J, Norton L, Albanell J, Kim YM, Mendelsohn J. Recombinant humanized anti-HER2 antibody (Herceptin) enhances the antitumor activity of paclitaxel and doxorubicin against HER2/neu overexpressing human breast cancer xenografts. Cancer Res 1998;58:2825–31.

2. Muss HB, Thor AD, Berry DA, et al. C-Erbb-2 Expression and response to adjuvant therapy in women with node-positive early breast-cancer. N Eng J Med 1994;330:1260–6.

3. Ligibel JA, Winer EP. Trastuzumab/chemotherapy combinations in metastatic breast cancer. Semin Oncol 2002;29:38–43.

4. Slamon DJ, Leyland-Jones B, Shak S, et al. Use of chemotherapy plus a monoclonal antibody against HER2 for metastatic breast cancer that overexpresses HER2. N Engl J Med 2001;344:783–92.

5. Natali PG, Nicotra MR, Bigotti A, et al. Expression of the p185 encoded by HER2 oncogene in normal and transformed human tissues. Int J Cancer 1990;45:457–61.

6. Press MF, Slamon DJ, Flom KJ, Park J, Zhou JY, Bernstein L. Evaluation of HER-2/neu gene amplification and overexpression: comparison of frequently used assay methods in a molecularly characterized cohort of breast cancer specimens. J Clin Oncol 2002;20:3095–105.

7. Niehans GA, Singleton TP, Dykoski D, Kiang DT. Stability of HER-2/neu expression over time and at multiple metastatic sites. J Natl Cancer Inst 1993;85:1230–5.

8. De Santes K, Slamon D, Anderson SK, et al. Radiolabeled antibody targeting of the HER-2/neu oncoprotein. Cancer Res 1992;52:1916–23.

9. Kotts CE, Su FM, Leddy C, et al. 186Re-labeled antibodies to p185HER2 as HER2-targeted radioimmunopharmaceutical agents: comparison of physical and biological characteristics with 125I and 131I-labeled counterparts. Cancer Biother Radiopharm 1996;11:133–44.

10. Palm S, Enmon RM Jr, Matei C, et al. Pharmacokinetics and Biodistribution of (86)Y-Trastuzumab for (90)Y Dosimetry in an Ovarian Carcinoma Model: Correlative MicroPET and MRI. J Nucl Med 2003;44:1148–55.

11. Horak E, Hartmann F, Garmestani K, et al. Radioimmunotherapy targeting of HER2/neu oncoprotein on ovarian tumor using lead-212-DOTA-AE1. J Nucl Med 1997;38:1944–50.

12. Geerlings MW, Kaspersen FM, Apostolidis C, van der Hout R. The feasibility of 225Ac as a source of alpha-particles in radioimmunotherapy. Nucl Med Commun 1993;14:121–5.

13. McDevitt MR, Ma D, Simon J, Frank RK, Scheinberg DA. Design and synthesis of 225Ac radioimmunopharmaceuticals. Appl Radiat Isot 2002;57:841–7.

14. Borchardt PE, Yuan RR, Miederer M, McDevitt MR, Scheinberg DA. Targeted actinium-225 in vivo generators for therapy of ovarian cancer. Cancer Res 2003;63:5084–90.

15. Sgouros G, Ballangrud AM, Jurcic JG, et al. Pharmacokinetics and dosimetry of an alpha-particle emitter labeled antibody: 213Bi-HuM195 (anti-CD33) in patients with leukemia. J Nucl Med 1999;40:1935–46.

16. Jurcic JG, Larson SM, Sgouros G, et al. Targeted alpha particle immunotherapy for myeloid leukemia. Blood 2002;100:1233–9.

17. Kennel SJ, Chappell LL, Dadachova K, et al. Evaluation of 225Ac for vascular targeted radioimmunotherapy of lung tumors. Cancer Biother Radiopharm 2000;15:235–44.

18. McDevitt MR, Ma D, Lai LT, et al. Tumor therapy with targeted atomic nanogenerators. Science 2001;294:1537–40.

19. Miederer M, McDevitt MR, Sgouros G, Kramer K, Cheung NK, Scheinberg DA. Pharmacokinetics, dosimetry, and toxicity of the targetable atomic generator, 225Ac-HuM195, in nonhuman primates. J Nucl Med 2004;45:129–37.

20. Sutherland RM. Cell and environment interactions in tumor microregions: the multicell spheroid model. Science 1988;240:177–84.

21. Yuhas JM, Li AP, Martinez AO, Ladman AJ. A simplified method for production and growth of multicellular tumor spheroids. Cancer Res 1977;37:3639–43.

22. Ballangrud AM, Yang WH, Dnistrian A, Lampen NM, Sgouros G. Growth and characterization of LNCaP prostate cancer cell spheroids. Clin Cancer Res 1999;5:3171s–6s.

23. Kolbert KS, Sgouros G. Display and manipulation of SPECT and CT studies for radiolabeled antibody therapy [abstract]. Cancer Biother Radiopharm 1998;13:302.

24. Ballangrud AM, Yang WH, Charlton DE, et al. Response of LNCaP spheroids after treatment with an alpha-particle emitter (213Bi)-labeled anti-prostate-specific membrane antigen antibody (J591). Cancer Res 2001;61:2008–14.

25. Nikula TK, McDevitt MR, Finn RD, et al. Alpha-emitting bismuth cyclohexylbenzyl DTPA constructs of recombinant humanized anti-CD33 antibodies: pharmacokinetics, bioactivity, toxicity and chemistry. J Nucl Med 1999;40:166–76.

26. Barendsen GW, Beusker TLJ, Vergroesen AJ, Budke L. Effect of different ionizing radiations on human cells in tissue culture. 2. Biological Experiments. Radiat Res 1960;13:841–9.

27. Sgouros G. Plasmapheresis in radioimmunotherapy of micrometastases: a mathematical modeling and dosimetrical analysis [see comments]. J Nucl Med 1992;33:2167–79.

28. DeNardo GL, Maddock SW, Sgouros G, Scheibe PO, DeNardo SJ. Immunoadsorption: an enhancement strategy for radioimmunotherapy. J Nucl Med 1993;34:1020–7.

29. Pimm MV, Andrew SM, Baldwin RW. Blood and tissue kinetics of radiolabelled anti-CEA monoclonal antibody and F(ab)2 and Fab fragments in nude mice with human tumour xenografts: implications for tumour imaging and radioimmunotherapy. Nucl Med Commun 1989; 10:585–93.

30. Lewis GD, Figari I, Fendly B, et al. Differential responses of human tumor cell lines to anti-p185HER2 monoclonal antibodies. Cancer Immunol Immunother 1993;37:255–63.

31. Shepard HM, Lewis GD, Sarup JC, et al. Monoclonal antibody therapy of human cancer: taking the HER2 protooncogene to the clinic J Clin Immunol 1991;11:117–27.

32. van Osdol W, Fujimori K, Weinstein JN. An analysis of monoclonal antibody distribution in microscopic tumor nodules: consequences of a "binding site barrier". Cancer Res 1991;51:4776–84.

33. Durand RE, Olive PL. Resistance of tumor cells to chemo- and radiotherapy modulated by the three-dimensional architecture of solid tumors and spheroids. Methods Cell Biol 2001;64:211–33.

34. Dean GS, Pusztai L, Xu FJ, et al. Cell surface density of p185(c-erbB-2) determines susceptibility to anti-p185(c-erbB-2)-ricin A chain (RTA) immunotoxin therapy alone and in combination with anti-p170(EGFR)-RTA in ovarian cancer cells. Clin Cancer Res 1998;4:2545–50.